Coordination Chemistry Reviews 536 (2025) 216644

Contents lists available at ScienceDirect

Coordination Chemistry Reviews

journal homepage: www.elsevier.com/locate/ccr

Lanthanide-doped nanoprobes for microRNA detection

Yunya Liu [a], Yin Huang [b], Yijun Luo [c], Yuxia Luo [c], Lijun Jiang [d], David Gallego-Ortega [e,*], Yuen Yee Cheng [f,*], Philip A. Gale [b,*], Guochen Bao [b,f,**]

[a] National Clinical Research Center for Geriatric Disorders, Xiangya Hospital, Central South University, Changsha, Hunan, China
[b] School of Mathematical and Physical Sciences, Faculty of Science, University of Technology Sydney, Sydney, New South Wales 2007, Australia
[c] College of Bioresources Chemical and Materials Engineering, Shaanxi University of Science & Technology, Xi'an 710021, Shaanxi, China
[d] Key Laboratory of Pesticide & Chemical Biology of Ministry of Education, Hubei Key Laboratory of Genetic Regulation and Integrative Biology, School of Life Sciences, Central China Normal University, Wuhan 430079, China
[e] School of Biomedical Engineering, University of Technology Sydney, Sydney, NSW 2007, Australia
[f] Institute for Biomedical Materials and Devices (IBMD), Faculty of Science, University of Technology Sydney, Sydney, New South Wales 2007, Australia

ARTICLE INFO

Keywords:
Upconversion nanoparticles
MicroRNA
Optical materials
Lanthanide materials
Disease diagnosis

ABSTRACT

MicroRNAs (miRNAs), a sub-class of non-coding RNAs approximately 20–24 nucleotides in length, have emerged as valuable biomarkers for disease diagnosis and prognosis, and potential forensic evidence. Advances in lanthanide-doped nanoprobes offer great promise for sensitive miRNA detection due to their high photostability, long luminescence lifetimes, and large anti-Stokes shifts. This review provides a comprehensive overview of strategies for developing lanthanide-doped nanoparticle (LnNP)-based biosensors for miRNA detection. We begin by introducing miRNAs as biomarkers in disease diagnostics and discussing synthesis and surface modification approaches for upconversion nanoprobes. We then highlight various detection strategies using lanthanide-doped nanoprobes—including clustered regularly interspaced short palindromic repeats (CRISPR)-based, sandwich structure-based, energy transfer-based, and inductively coupled plasma (ICP)-based detection. Finally, we address current challenges, potential applications and future perspectives for LnNP-based biosensors and their potential for clinical translation.

1. Introduction

MicroRNAs (miRNAs) are a sub-class of non-coding RNAs, typically 20–24 nucleotides long, recognized for their high sequence homology [1]. They are estimated to regulate over 60 % of human genes [2] and play essential roles in various developmental and pathological processes [3]. Since their stable presence in plasma was first detected in 2008 [4], miRNAs have garnered significant attention due to their specific expression patterns in diseases. The 2024 Nobel Prize in Physiology or Medicine was awarded to Victor Ambros and Gary Ruvkun for their pioneering work in discovering microRNA and its function in post-transcriptional gene regulation [5]. Extensive research has highlighted their potential as an early stage diagnostic biomarker [6–8], as well as their utility in disease prognosis [9–11] and forensic evidence [12–14]. While traditional miRNA detection methods such as real-time quantitative reverse transcription PCR (qRT-PCR) [15], digital PCR (dPCR) [16,17], microarray [18], and Northern blot [19], serve current research needs [20], there is an urgent demand for new, rapid, and accurate miRNA detection platforms to facilitate broader applications in clinical and forensic settings.

With the rapid advancements in materials science and optics, new strategies for miRNA detection been emerged, leveraging organic dyes [21], quantum dots (QDs) [22], gold nanoparticles (AuNPs) [23], and lanthanide hybrids [24]. Among these, lanthanide-doped nanoparticles have gained prominence as sensitive nanoprobes for miRNA detection due to their exceptional optical properties, including high photostability, long luminescence lifetimes, and large anti-Stokes shifts [25–29]. Lanthanide-doped nanophotonic particles are capable of converting multiple low-energy near-infrared photons into high-energy visible and ultraviolet emissions [30–35]. Their considerable anti-

* Corresponding author.
** Corresponding author at: School of Mathematical and Physical Sciences, Faculty of Science, University of Technology Sydney, Sydney, New South Wales 2007, Australia.
E-mail addresses: david.gallegoortega@uts.edu.au (D. Gallego-Ortega), yuenyee.cheng@uts.edu.au (Y.Y. Cheng), philip.gale@uts.edu.au (P.A. Gale), guochen.bao@uts.edu.au (G. Bao).

https://doi.org/10.1016/j.ccr.2025.216644
Received 16 November 2024; Received in revised form 12 March 2025; Accepted 16 March 2025
Available online 3 April 2025

Stokes shift effectively eliminates background noise from sample autofluorescence and light source interference, greatly enhancing biomarker detection sensitivity. The long luminescent lifetimes of lanthanide materials (microsecond to millisecond) [36] allow for time-resolved techniques [37–39] to eliminate the short-lived fluorescence background from biological samples (which typically occur in nanoseconds). By introducing a delay between the excitation pulse and the emission signal, this method can further improve detection sensitivity [40].

In this review, we explore strategies for developing LnNP-based biosensors for miRNA detection and their potential biomedical applications (Fig. 1). We begin by introducing miRNAs as biomarkers for disease diagnostics and the traditional detection methods such as PCR (qRT-PCR, dPCR), microarray, and Northern blot. Next, we survey synthetic approaches and surface modification techniques for creating bright, biocompatible upconversion nanoprobes. We then delve into various detection strategies utilizing lanthanide-doped nanoprobes, including CRISPR-based methods, sandwich-structure-based detection, energy transfer-based detection, and ICP-based detection. Finally, we address the challenges, potential applications of LnNP-based biosensors, along with future perspective for their clinical translation.

2. miRNA: From discovery to their use as biomarkers

2.1. miRNA

MicroRNAs (miRNAs) were first discovered in *Caenorhabditis elegans* by scientists Victor Ambros and Gary Ruvkun in 1993 [5]. The *lin-4* in *C. elegans* produces a transcript of about 22 nucleotides that does not encode a protein but instead pairs with the 3' untranslated region of the *lin-14* mRNA, thereby negatively regulating the level of LIN-14 protein [5,41]. In 2003, Victor Ambros introduced a standardized system for miRNA annotation [42]. Since then, an increasing number of miRNAs have been identified across animals, plants, and viruses [43–45]. As of 2024, the miRBase [46], a leading online repository for miRNA data, includes over 48,000 mature miRNA sequences from 271 organisms. Research estimates that miRNAs regulate approximately 60 % of human genes [2].

The maturation of miRNA involves several proteins. The process typically begins with RNA polymerase II (Pol II) transcribing primary miRNAs (pri-miRNAs) in the nucleus, which are several thousand nucleotides long and possess a stem-loop structure. In the second step, the pri-miRNA is cleaved by the nuclear RNase III enzyme Drosha and its cofactor DGCR8, producing a precursor miRNA (pre-miRNA) of approximately 70 nucleotides [47]. Pre-miRNAs are then transported into the cytoplasm by exportin-5 proteins [48]. In the third step, the pre-miRNA is further cleaved by the ribonuclease III enzyme Dicer, generating one or two mature miRNAs, each about 22 nucleotides in length [49]. Mature miRNAs are subsequently loaded onto Argonaute proteins to form the RNA-induced silencing complex [50], which protects miRNAs from degradation by various ribonucleases, giving them an average half-life of about five days, and making them more stable than mRNA [51]. In addition to Argonaute proteins loading, some extracellular miRNAs bind to lipoproteins [52], while a small portion are encapsulated in exosomes [53], both mechanisms providing protection against nuclease activity.

MicroRNA serves as post-transcriptional regulators, targeting mRNA through three primary mechanisms. The first mechanism involves cleaving the mRNA into two segments, the second entails removal of the 3' poly(A) tail or 5' cap, leading to destabilization of the mRNA. The third mechanism prevents the translation of mRNA into proteins [54]. miRNAs are involved in nearly all physiological and pathological processes in humans. Their physiological roles include regulating cell proliferation, differentiation, apoptosis, and circadian rhythms [55,56], while their involvement in pathological processes encompasses cancer, immune system disorders, genetic diseases, obesity, and cardiovascular conditions [57–59].

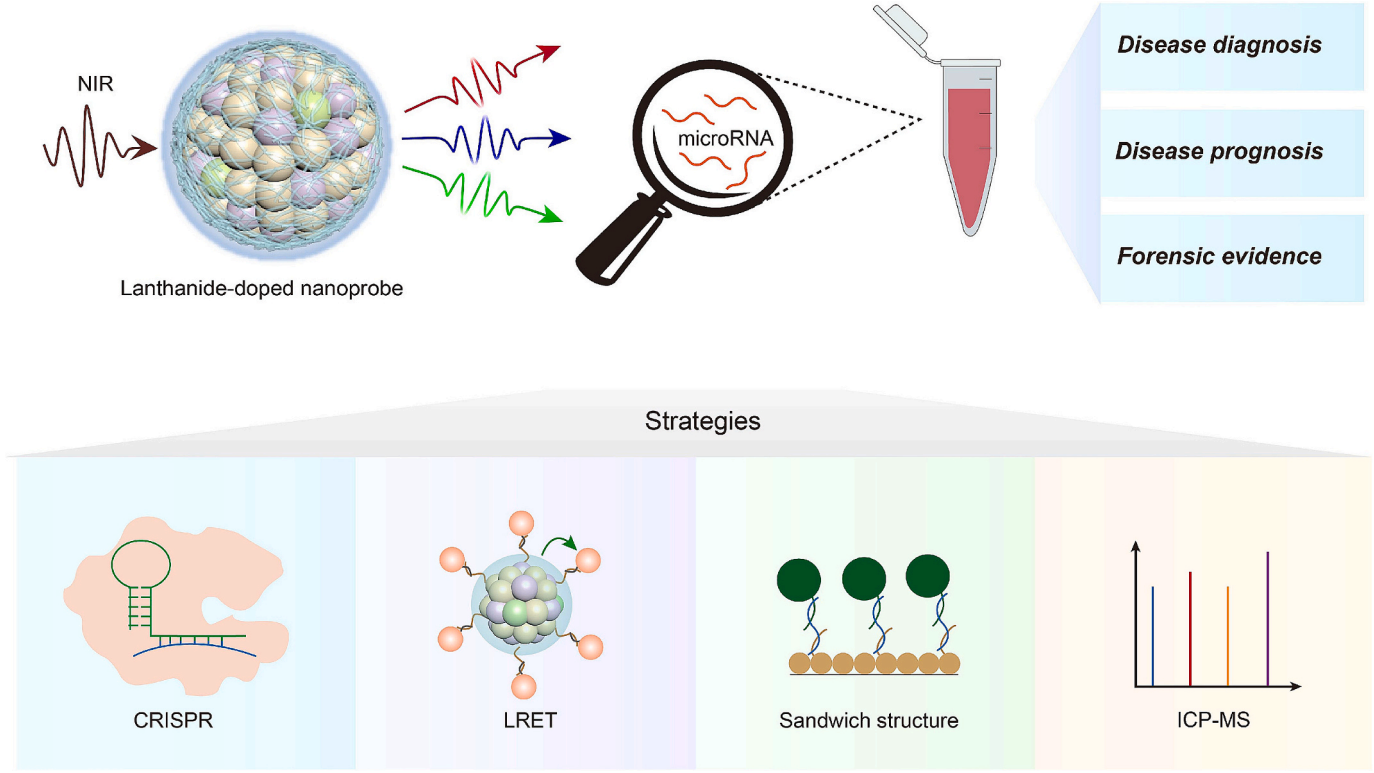

Fig. 1. Illustration of lanthanide-doped nanoprobes for microRNA detection and their strategies. CRISPR, clustered regularly interspaced short palindromic repeats; LRET, luminescence resonance energy transfer; ICP-MS, inductively coupled plasma-mass spectroscopy.

2.2. miRNAs as biomarkers

Several key discoveries have challenged previous misconceptions about miRNA stability, which were largely based on the susceptibility of mRNA to degradation [60,61]. In 2008, Lawrie et al. detected specific miRNAs in the serum of patients with diffuse large B-cell lymphoma, finding significantly elevated levels compared to healthy controls [6]. Around the same time, Chen et al. found that miRNAs were stably present in the serum and plasma of both humans and animals [4]. They also identified distinct miRNA expression profiles in patients with non-small cell lung cancer, colorectal cancer, and type 2 diabetes compared to healthy donors [4]. Another study showed that miRNAs in human plasma exist in a remarkably stable form, protected from endogenous RNase activity [8]. These findings supported the idea that miRNAs could serve as potential biomarkers for cancer and other diseases, paving the way for further research into circulating miRNAs as diagnostic tools.

The miRNAs were detected in various body fluids, including urine, saliva, milk, cerebrospinal fluid, and amniotic fluid [7]. A substantial amount of clinical validation data suggests that many diseases exhibit unique miRNA profiles that can differentiate patients from healthy individuals. For instance, four specific miRNAs (miR-1290, miR-125a, miR-125b, and miR-1298) in cerebral spinal fluid were shown to accurately distinguish patients with Medulloblastoma from healthy individuals [62]. In another study involving 100 serum samples, miR-122 and miR-224 in plasma were able to differentiate early hepatocellular carcinoma from chronic hepatitis and healthy volunteers, with sensitivities of 87.5 % and 92.5 %, respectively, which are higher than the sensitivity of alpha-fetoprotein, current at 57.5 % [63]. Alpha-fetoprotein is used as a tumor biomarker in clinical practice.

Studies have shown that miRNAs are stable in blood. For instance, plasma stored at −80 °C for 12 months showed no significant changes in the levels of eight miRNAs compared to pre-freezing levels, and miR-212-3p remained stable even after 14 years of storage [64]. Additionally, continuous monitoring of plasma miRNAs in 22 healthy individuals over three months revealed consistent expression levels [65]. Given their stability in bodily fluids and the ease of sampling, which can be minimally invasive or even non-invasive, miRNAs hold great potential as valuable biomarker for disease diagnosis.

2.3. Conventional methods for miRNA detection

Traditional methods for miRNA detection include Northern blot, microarray technology, and PCR (qRT-PCR and dPCR), with further details provided in Box 1. Additionally, next-generation sequencing is used for the detection of miRNAs, greatly expanding the detection range and sensitivity of miRNAs. However, due to the fact that this technology requires professional personnel to complete and has high requirements for instruments and analytical techniques, these factors limit its promotion in detection [66,67]. While these conventional methods meet certain research needs, they also have significant limitations (Box 1). Therefore, the development of new miRNA detection technologies is crucial. In recent years, advancements in materials science and optics, particularly the introduction of lanthanide probes, have offered promising solutions to these challenges and opened up new possibilities for the application of miRNA in clinical diagnosis.

3. Lanthanide-doped nanoparticles

Lanthanide-doped upconversion nanoparticles (UCNPs) are inorganic nanomaterials [70] with notable advantages over conventional organic dyes and semiconductor quantum dots, including large anti-Stokes shifts [71], long luminescence lifetime, low photobleaching, and improved tissue penetration [72]. The most remarkable optical feature of UCNPs is the anti-Stokes luminescence, where near infrared light is absorbed and converted into light with wavelengths in ultraviolet and visible region [26,35,73,74]. These exceptional optical properties render these probes highly useful in background-free and photostable biosensing [75].

3.1. Composition and upconversion mechanisms

Typically, UCNPs are composed of an inorganic matrix, a sensitizer and an activator. The matrix provides a stable crystalline framework that supports both sensitizer and activator [30]. The sensitizer absorbs photons and transfers energy to the activator through a multiphoton process, with the activator serving as the luminescent center of the UCNPs [76]. Common host materials include $NaYF_4$ [32,35], $NaGdF_4$ [77], $NaLuF_4$ [78], Y_2O_3 [79], Ba_2GdF_7 [80], and $LiBaF_3$ [81]. Yb^{3+} is typically used as a sensitizer due to its broad absorption around 980 nm and simple energy level. It can efficiently transfer energy to activators such as Er^{3+}, Tm^{3+}, Ho^{3+} [82,83]. Nd^{3+} ions have also been employed as complementary sensitizers to extend absorption to 808 nm [84].

Upconversion processes mainly follow three luminescence mechanisms: excited state absorption (ESA), energy transfer upconversion (ETU) [85], and photon avalanche (PA) upconversion. In ESA, a sequential absorption of photons occurs within one ion. An electron is

Box 1
The conventional methods for miRNA detection.

a. Northern blot. Northern blot is one of the earliest techniques used for miRNA detection [19]. This method involves separating miRNAs by molecular weight through electrophoresis, transferring them to a membrane, and detecting with probes that are complementary to the target miRNA. These probes are typically labeled with either radioactive or non-radioactive markers, and after hybridization, miRNA expression levels are determined by measuring the signal. However, Northern blot has low sensitivity, requires large amounts of miRNA, and is both labor-intensive and time-consuming.

b. Microarray technology. Microarray technology starts by immobilizing oligonucleotide probes that are complementary to known miRNA onto a chip. The miRNAs from the sample are then labeled with a fluorescence dye, such as cyanine 3-cytidine bisphosphate (pCp-Cy3) [18]. The labeled miRNAs are hybridized to the chip overnight through base pairing and the fluorescence intensity in each well is measured using a microarray scanner. This technique is effective for large-scale expression profiling, but it is limited to detecting only known miRNAs [68]. Additionally, its relatively low sensitivity, low specificity and low repeatability limit its application [69].

c. qRT-PCR. Real-time quantitative reverse transcription PCR (qRT-PCR) is considered the gold standard for miRNA detection. The process involves converting miRNA into complementary DNA (cDNA) via reverse transcription, followed by real-time amplification using specific primers. During amplification, miRNA expression is quantified using fluorescent dyes, such as SYBR Green [15]. QRT-PCR provides high sensitivity and quantitative accuracy, but it has significant limitations in terms of time and cost. Additionally, designing specific primers and probes can be challenging, especially for miRNAs that are closely related within the same families. Although the third-generation PCR, digital PCR (dPCR), achieves absolute quantification of miRNA, it has the limitations of time and cost [16].

first promoted to a metastable excited state (E1) upon absorption of a photon, then further excited to a higher energy state (E2) by absorbing a second photon, before decaying back to the ground state [86]. The ETU mechanism, in contrast, relies on a nearby sensitizer. The sensitizer absorbs photon and transfers energy to the activator, sequentially populating the activator's metastable excited state (E1) and higher excited state (E2) to generate upconversion luminescence [30]. ETU is generally more efficient than ESA. The PA mechanism combines both ESA and energy transfer processes. Initially, ion 1 is excited from the ground state to E1 via weak, non-resonant absorption. ESA then promotes ion 1 to the higher excited state E2. A resonant cross-relaxation between the super-excited ion 1 (at E2) and a nearby ion 2 (in the ground state) results in both ions being in the E1 state. Subsequently, the ion 2 then transfers the energy to ion 1, forming a complete loop. In this looping process, very little upconversion is produced below the threshold, while the upconversion emission intensity increases by orders of magnitude above the threshold [87,88].

Due to the forbidden f–f transitions of Ln^{3+}, lanthanide materials typically exhibit low brightness due to their low absorption coefficients [30]. Several strategies have been proven effective in enhancing the emission intensity of upconversion nanoparticles, including core-shell structures, dye sensitization, high excitation densities, and superlensing effects. By growing an inert shell around an active core, surface quenching can be suppressed, thereby enhancing the luminescence of the core-shell nanoparticle [89]. Due to their higher absorption capacity, organic dyes have been employed to enhance the emission intensity of lanthanide nanoparticles [32,35]. High-excitation irradiance has also been reported to mitigate concentration quenching in Tm^{3+}-doped upconversion nanoparticles as the Tm^{3+} concentration increases from 0.5 to 8 mol% [90]. Additionally, the superlensing effect of dielectric microbeads has been employed to substantially enhance photon upconversion in lanthanide-doped nanocrystals [91].

3.2. Optical properties for detection

UCNPs exhibit distinctive optical properties that distinguish them from organic fluorescent dyes [92–94], fluorescent proteins [95,96] and quantum dots [97,98] as probes for biomedical usages. Their large anti-Stokes shift effectively minimizes background noise from sample autofluorescence and light source interference, significantly improving biomarker detection sensitivity. Additionally, their long luminescent lifetimes (ranging from microseconds to milliseconds) facilitate time-gated techniques, which can suppress the short-lived fluorescence background of biological samples (in nanoseconds) by introducing a delay between the excitation pulse and the emission signal, and improve detection sensitivity.

The 4f-4f transitions (electronic transitions within the 4f orbitals) within lanthanide ions render them highly resistant to photobleaching, even under intense laser excitation, making them particularly attractive as sensing probes for biomarkers. By adjusting the type, ratio, and concentration of doped rare earth elements, multi-colour luminescence can be achieved under a single excitation source [99,100]. This property enables the simultaneous detection of multiple biological substances. Moreover, near-infrared light, used as the excitation source, exhibits low absorption and scattering in biological samples, allowing for deeper tissue penetration compared to visible and ultraviolet light, making it particularly suitable for applications in biological systems [101].

3.3. Synthetic strategy

Synthesis methods are crucial for the application of UCNPs in bioassays. For UCNPs to be effectively used in biomedical applications, they must not only have the appropriate size but also exhibit strong luminescence intensity. Synthesis methods will influence key properties such as morphology, size [102], structure, and crystal phase, which in turn affect UCNP luminescence. In this section, we summarize five common methods used for synthesizing UCNPs, including thermal decomposition method, hydrothermal/solvothermal method, co-precipitation method, sol-gel method, and microwave assisted method. These synthetic methods can yield high-performance UCNPs suitable for use as nanoprobes in miRNA detection.

3.3.1. Thermal decomposition method

Thermal decomposition method involves dissolving the precursor in a high-boiling organic solvent, followed by high-temperature decomposition of the precursor to synthesize UCNPs. Common rare-earth organic precursors include trifluoroacetate, oleate, and acetate. Frequently used high-boiling organic solvents in this method are oleic acid, 1-octadecene, and oleylamine. 1-octadecene, with a boiling point above 300 °C, provides the necessary high-temperature environment for the reaction. Oleic acid and oleylamine, with their long alkyl chains, serve as surfactants. They prevent the agglomeration of nanocrystals during the reaction process and also regulate the size and morphology of nanoparticles by selectively adsorbing onto specific crystal surface [75].

3.3.2. Hydrothermal/solvothermal method

The hydrothermal/solvothermal method utilizes water or organic solvent as the reaction medium to promote the slow growth of nanocrystals within a closed system under high temperature and high pressure conditions [103]. Typically, the reaction is carried out in a stainless-steel reactor equipped with a protective lining, which ensures the necessary temperature and pressure stability for the synthesis process. Unlike thermal decomposition, this method can be carried out at relatively low reaction temperatures, typically ranging from 160 to 220 °C [104]. To produce nanoparticles with desired shapes and surface capping agents, cetyltrimethylammonium bromide [105] and ethylenediamine tetraacetic acid [106] are commonly employed in this process.

3.3.3. Co-precipitation method

The co-precipitation method is considered one of the most convenient and user-friendly approaches for synthesizing UCNPs, as it does not require expensive equipment, harsh reaction conditions, or complicated procedures. The process involves dissolving the precursors in a solvent to create a solution containing one or more types of ions. After the precipitation step, an appropriate precipitant is gradually added to form an insoluble co-precipitate, from which the desired nanocrystals are obtained through post-treatment. This method operates at a relatively low synthesis temperature and produces products with high purity [106,107].

3.3.4. Sol-gel method

The sol-gel method is a wet chemical strategy for preparing inorganic materials through inorganic polymerization. Initially, inorganic or metal salts serve as precursors, which are thoroughly mixed in a liquid phase. A specific additive is then introduced to initiate hydrolysis and condensation chemical reaction, resulting in formation of a stable sol system. The gel particles undergo gradual polymerization, leading to the formation of a gel after ageing. Finally, the nanoparticles are obtained by drying and sintering the gel [108].

3.3.5. Microwave-assisted method

Microwave-assisted synthesis is a technique for rapidly heating solutions and reactants. This approach typically encompasses both solid microwave and liquid microwave synthesis methods. In the solid microwave method, rare earth oxides are mixed with ammonium hydrogen fluoride and ammonium fluoride, allowing for the direct synthesis of nanoparticles under microwave irradiation. In the liquid microwave synthesis method, rare earth salts and fluorides are dissolved in a solvent, and upon heating with microwaves, they react to form nanoparticles [109].

3.4. Surface modifications

The surfaces of UCNPs synthesized by the aforementioned methods typically contain numerous hydrophobic ligands, resulting in poor water solubility and biocompatibility, which significantly limits their application in biological systems. Therefore, the functional modification of the UCNPs surface is essential for their uses in the biomedical field. Several strategies are employed to modify UCNPs, including ligand removal, ligand exchange, ligand oxidation, layer-by-layer self-assembly, and amphiphilic polymer encapsulation and surface silication (Fig. 2).

3.4.1. Ligand removal

Ligand removal is a straightforward and effective strategy for modifying UCNPs. The method involves removing the oleic acid ligand from the surface of UCNPs using hydrochloric acid and ethanol under sonication. In a low pH environment, the oleic acid ligands can gradually be protonated, allowing them to dissociate from the nanoparticles and exposing the rare earth ions for subsequent modification. Ethanol can be used as a cleaning solvent to further eliminate residual impurities and unbound ligands. For instance, Hao et al. [110] used this approach to prepare a csUCNP/Au-Au sensor for detecting long-chain oligonucleotides of SARS-CoV-2 N-gene. Additionally, an ultrasonic separation method can be employed to remove oleate ligands from the nanoparticle surface, leveraging the principle of surface absorption at moderate ultrasonic power [111].

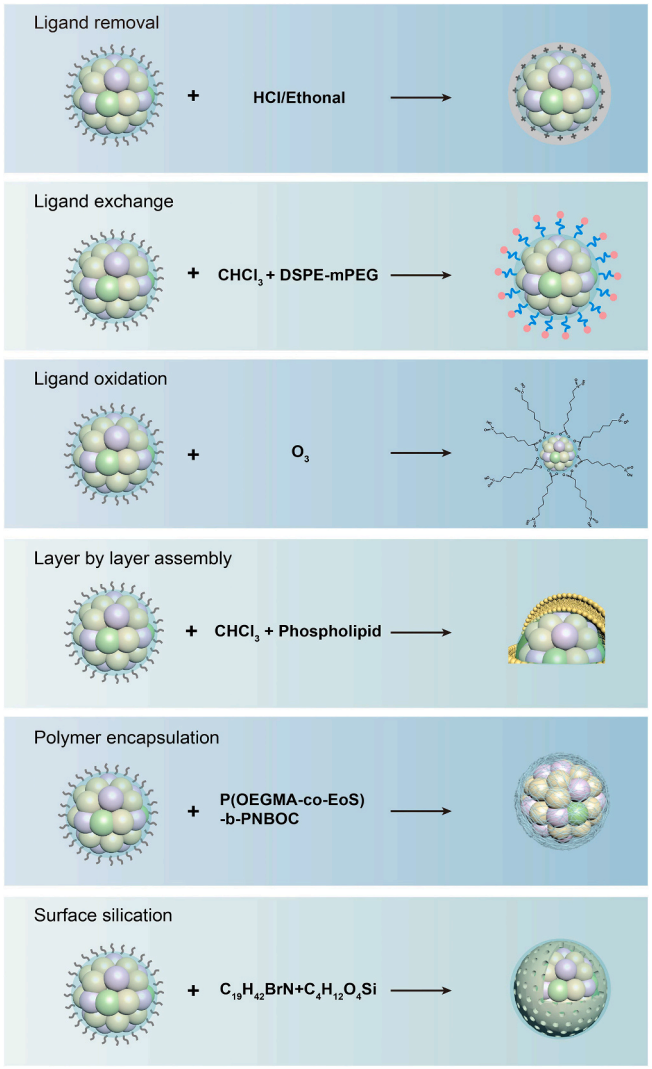

Fig. 2. Illustration of surface modification strategies of UCNPs.

3.4.2. Ligand exchange

In ligand exchange strategy, the original hydrophobic ligands on the surface of UCNPs are replaced with organic ligands that possess strong coordination capabilities and hydrophilicity. This method enhances the hydrophilicity of UCNPs while preserving the morphology of the nanoparticles. Common ligands used in this process include citric acid, sodium alginate, and polyethylene glycol. For instance, Diego Mendez-Gonzalez et al. [112] employed polyacrylic acid to replace the hydrophobic ligand system via ligand exchange method, and prepared single-stranded DNA-UCNPs sensor for detecting miR-21-5p DNA-analogues.

3.4.3. Ligand oxidation

This method employs strong oxidants (e.g. O_3/Lemieux-von Rudloff) to oxidize the carbon-carbon double bonds of the oleic acid ligands on the surface of UCNPs into a carboxyl group, thereby rendering UCNPs hydrophilic [113,114]. The presence of free carboxylic acid groups enables further bio-functionalization with a variety of biomolecules [115]. However, this method is primarily applicable to ligands such as oleic acid or linoleic acid that contain carbon-carbon double bonds. Additionally, it may lead to a reduction in the luminescence intensity of the nanoparticles, presenting certain limitations.

3.4.4. Layer by layer assembly

The layer-by-layer assembly method can be used to modify the UCNP surfaces through electrostatic adsorption, hydrogen bonding, ligand bonding and chemical bonding. The method enables precise control over the thickness of the coated material and can be applied to nanomaterials of different shapes and sizes. For example, Zhou et al. [116] coated hydrazine (N_2H_4) and anthocyanin dye (Cypate) sequentially on the surface of UCNPs, and conjugated the interfering RNA gene (HSP70-siRNA) to the porous UCNPs, leading to the preparation of UCNP-cy-siRNA with a significant anti-tumor efficacy. Similarly, Liu et al. [117] utilized this method to develop pH-responsive UCNP@2xCe6-DMMA-PEG sensors by loading multilayer Chlorin e6 (Ce6) polymers onto UCNPs. Additionally, Gao et al. prepared upconversion nano-jelly hydrogels (UCNJs) using this method for cancer diagnosis and treatment [118].

3.4.5. Polymer encapsulation

The principle of polymer encapsulation involves combining the hydrophobic molecules on the surface of UCNPs with the hydrophobic end of an amphiphilic polymer to form an inner layer, while the hydrophilic end of the amphiphilic polymer forms an outer layer. This structure enhances the dispersion of nanoparticles in aqueous solution. Xu et al. [119] prepared UCNP@TTD-cRGD nanoparticles using amphiphilic polymer (DSPE-PEG-MAL), which can be used for photodynamic therapy. Similarly, Ju et al. [120] utilized an amphiphilic polymer (*P*(OEGMA-*co*-EoS)-*b*-PNBOC) to encapsulate UCNPs, and prepared vesicles suitable for tumor treatment.

3.4.6. Surface silication

Silicon dioxide coating is a widely used strategy for modifying UCNPs. The UCNPs surface can be coated with a controllable thickness of mesoporous silica ($mSiO_2$) using either the reverse microemulsion method or Stöber method. The resulting UCNPs@$mSiO_2$ are more amenable to functional group modification, and their porous structure allows for drugs loading, making them suitable for biomedical applications. For instance, Wang et al. [121] developed microneedle patches for transdermal delivery of siRNAs. This system utilizes hyaluronic acid as a matrix, with mesoporous silica-coated UCNPs (UCNPs@$mSiO_2$) serving as a loading carrier for siRNA.

4. LnNP-based biosensor for miRNA detection

The unique advantages of lanthanide-doped nanoparticles have garnered significant interest among researchers. Although this field is still in its infancy, it has demonstrated potential for miRNA detection, especially regarding sensitivity and specificity. In this section, we explore various miRNA detection strategies utilizing LnNP-based biosensors, including CRISPR-based miRNA detection, sandwich structure-based miRNA detection, energy transfer-based miRNA detection, and ICP-based miRNA detection.

4.1. CRISPR-based miRNA detection

4.1.1. CRISPR

The CRISPR system is an adaptive immune defense found in most bacteria and archaea [122], first discovered in *Escherichia coli* in 1987 [123]. It is divided into two categories: Class I and Class II. Class II is the most widely used due to its powerful functionality, requiring only simple CRISPR proteins and CRISPR-related RNA (crRNA), while Class I relies on the cooperation of multiple proteins. Class II includes Cas9, Cas12, Cas13 and Cas14. Among these, Cas9 has been extensively used in gene editing since 2013, for applications such as knock-out, knock-in, and point mutations [124,125]. Cas12, Cas13, and Cas14 are also widely used in biosensor detection platforms [126] due to their programmability, specificity, and collateral cleavage activity. Existing CRISPR-based detection platforms include HOLMES (a one-HOur Low-cost Multipurpose highly Efficient System) [127], DETECTR (DNA Endonuclease Targeted CRISPR *Trans* Reporter) [128], SHERLOCK (Specific High Sensitivity Enzymatic Reporter UnLOCKing) [129] and SHERLOCK V2 [130]. The HOLMES and DETECTR platforms are used for DNA and RNA detection, where Cas12a cleaves a quenched fluorescent single-stranded DNA (ssDNA) reporter, e.g. HEX-N12-BHQ1 (Hexachloro-fluorescein-[12-nucleotide sequence]-Black Hole Quencher 1), to generate a fluorescence signal following PCR or isothermal amplification, respectively [127,128]. SHERLOCK utilizes a Cas13a detection platform based on recombinase polymerase amplification and reverse transcription- recombinase polymerase amplification [129]. The SHERLOCK V2 platform allows for the simultaneous detection of multiple targets by employing various CRISPR family members, enabling the identification of mutations in dengue fever or Zika virus single-stranded RNA (ssRNA) as well as analysis of patient liquid biopsy samples through a lateral flow platform, eliminating the need for specialized detection equipment [130].

4.1.2. UCNP-based CRISPR in miRNA detection

The specific recognition and rapid collateral cleavage activity of the CRISPR family significantly enhance the specificity and sensitivity of nucleic acid detection. Combining UCNPs with CRISPR for miRNA detection creates an effective detection platform. Currently, several detection platforms have been developed that integrate lanthanide-doped nanoprobe technology with CRISPR, primary falling into two categories: Cas13-based miRNA detection platform utilizing UCNPs, and Cas12-based miRNA detection platform utilizing UCNPs. In this section, we describe and summarize the strategies from three perspectives: miRNA recognition, signal amplification, and detection reporting systems.

4.1.3. Cas13-based miRNA detection platform

Cas13a, paired with crRNA that matches the target miRNA, can directly recognize ssRNA without requiring a protospacer adjacent motif (PAM), making it an ideal miRNA recognizer [131]. The Cas13 family includes several variants, such as LwaCas13a, CcaCas13b, LbaCas13a, and PsmCas13b, each originating from different bacterial species and exhibiting unique preferences for cleavage at special di-nucleotide sites. For instance, PsmCas13b shows heighten sensitive to adenosine cleavage, while LwaCas13a prefers uracil ribonucleotides. [130]. To enhance signal amplification, a specially designed RNA hairpin known as Trigger, containing two uracil ribonucleotides in the loop, is utilized. Due to LwaCas13a's cleavage preference, the Trigger is cleaved into two specific single strands (Fig. 3a). This feature is also applied in multi-nucleic acid synchronous detection platforms. Given that miRNA levels in body fluids are typically low, detection is often coupled with amplification techniques.

Common methods for amplification include nicking enzyme amplification reaction (NEAR), catalytic hairpin assembly (CHA), strand displacement amplification (SDA), rolling circle amplification (RCA), and 3D walking nanomotor amplification. NEAR is a cyclic amplification method that utilizes a nicking enzyme to digest ssDNA at specific sites, creating a nick and releasing ssDNA fragments from double-stranded DNA (dsDNA). For example, the Trigger' binds to the toehold of the hairpin structure CH1, forming dsDNA. This dsDNA is then cleaved by the DNA nicking enzyme (Nb.BbVCI) at a designated site, releasing the Trigger', which is then involved in further cyclic amplification. Additionally, another ssDNA fragment is released, serving as a switch for the subsequent reporting system (Fig. 3a).

In this system, the reporting mechanism consists of Fe_3O_4@AuNPs modified with DNA1 and UCNPs modified with DNA2. DNA1 partially pairs with DNA2, resulting in the forming magnetic UCNPs. When the target miRNA is present, the ssDNA generated by the amplification system binds to DNA1 on magnetic UCNPs causing UCNPs to dissociate. After magnetic separation, a strong luminescent signal can be detected by irradiating the supernatant with a 980 nm laser (Fig. 3a). This system demonstrates a low limit of detection (LOD) of 83.2 fM (Fig. 3b) and high selectivity, capable of distinguishing between miRNAs that differ by as few as two bases (Fig. 3c) [132].

SDA is an in vitro isothermal amplification method that utilizes endonucleases to cleave DNA and generate new strands through the action of DNA polymerase. As the new strand is synthesized, it displaces the original strand, leading to the release of the old strand. For instance, as shown in Fig. 3d, when miRNA is present, Cas13a cleaves the hairpin structure RP, generating an ST strand that complements the template chain (TC) (Fig. 3d). Under the influence of DNA polymerase, the ST chain extends along the TC, forming dsDNA. At this stage, a nicking enzyme (NEase) recognizes the specific site on dsDNA and cleaves one of the single strands. DNA polymerase then continues extending along the TC, replacing the Trigger and releasing it for further amplification.

Some studies combine multiple amplification methods to enhance detection sensitivity. For example, integrating SDA with catalytic hairpin assembly allows the single-stranded product of SDA to serve as a trigger for CHA, initiating the opening of the hairpin structure H1. Once opened, H1 actives the subsequent opening of FAM-H2, a typical enzyme-free amplification method. This process causes FAM to move from the proximal to the distal end of UCNPs. Due to the distance between UCNPs and FAM exceeds 10 nm, the Förster Resonance Energy Transfer (FRET) is diminished, resulting in stronger upconversion luminescence signals (Fig. 3d). Additionally, photoelectrochemical biosensing has been incorporated into the reporting system. By constructing a p–n heterojunction using an n-type semiconductor (ZnO) and a p-type semiconductor ($CuInS_2$) beneath the UCNP layer, the system demonstrated excellent photoelectric conversion performance. This dual-signal biosensing method can detect both UCL and electrical signals, significantly enhancing sensitivity and accuracy. This approach minimizes false positives and improves analysis efficiency in complex biological environments. The system achieved a low LOD of 76.54 aM for near-infrared photoelectrochemistry detection (Fig. 3e) and 51.36 aM for UCL detection(Fig. 3f) [133].

4.1.4. Cas12-based miRNA detection platform

In the UCNP-based Cas12 miRNA detection platform, an ssDNA is designed to specifically recognize the target miRNA through complementary base pairing. This recognition leads to the formation of an ssDNA strand, which is identified by Cas12a with the assistance of

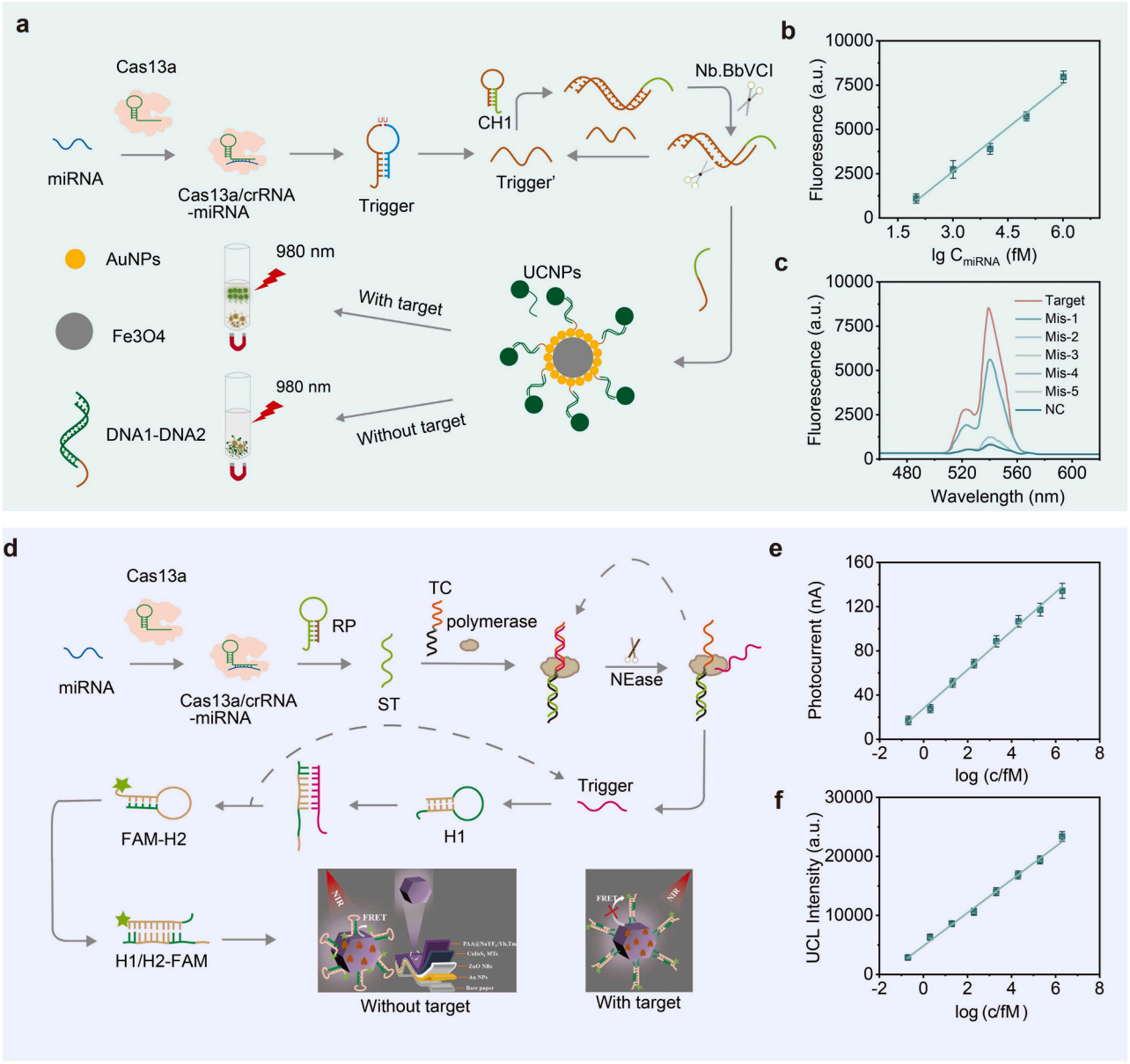

Fig. 3. UCNP-based CRISPR/Cas13a miRNA detection platforms. (**a**) Schematic illustration of miRNA detection method based on magnetic upconversion nanoparticle enhancement and CRISPR/Cas13a-driven signal amplification coupled with CHA. (**b**) Fluorescence intensity plotted against vary concentration of sja-miR-2c5p, with a LOD of 83.2 fM. (**c**) Fluorescence spectra of UCNPs in the supernatant after the addition of different crRNA and miRNA in a base mismatch experiment. crRNA-sja-miR-2c5p: 5'-CACAUCACAGUCGAACAAGGGU-3', sja-miR-2c5p: 3'-GUGUAGUGUCAGCUUGUUCCCA-5'. Mis-1, Mis-2, Mis-3, Mis-4, Mis-5 represent the number of mismatch base compared to crRNA-sja-miR-2c5p and sja-miR-2c5p, respectively. Adapted with permission from Ref. [132]; Copyright 2023 American Chemical Society. (**d**) Schematic illustration of miRNA detection based on FRET and CRISPR/Cas13a-driven signal amplification coupled with SDA and CHA. (**e**) Photocurrent measurements for various concentrations of miR-106a. (**f**) UCL emission for different concentrations of miR-106a. Adapted with permission from Ref. [133]; Copyright 2023 American Chemical Society. Nb.BbVCI, a DNA nicking enzyme; ST, single-stranded DNA; TC, template chain; CH1, RP, and H1, three different hairpin structures.

various nucleases, as Cas12 only exclusively recognizes ssDNA or dsDNA [134]. For example, a hairpin structure HP modified with a photochromic linker at the junction of its loop and stem is conjugated to the UCNP. Upon irradiation with a 980 nm laser, the photoresponsive linker opens, revealing the ssDNA that target miRNA. For signal amplification, exonuclease EXOIII was introduced into the system, EXOIII selectively digests one strand of dsDNA or DNA-RNA hybrids from the 3' to 5' end, releasing the miRNA along with another ssDNA strand know as Trigger. The released miRNA can then bind to another HP structure to initiate the first amplification.

This system also incorporates the RCA method. The Trigger links the 5' and 3' ends of the amplification template together, forming a circular template chain through T4 ligase. Subsequently, phi29 polymerase extended the Trigger based on this circular template (Fig. 4a). The template chain contains not only Trigger-binding fragments but also crRNA recognition sequences and PAM sequences (typically TTT). Cas12a utilizes its trans-cleavage capability to nonspecifically cleave the F-Q sequence, which is modified with quenching and fluorescence groups, such as BHQ-ssDNA-FAM, resulting in a strong luminescent signal at 510 nm. The trans-cleavage rate of Cas12a is remarkably high, functioning as a third round of amplification, with LbCas12a-crRNA bound to an ssDNA activator molecule catalyzing trans-ssDNA cleavage at a rate of ~250 per second [128]. This strategy achieves a LOD of 6.01 fM (Fig. 4b) [135].

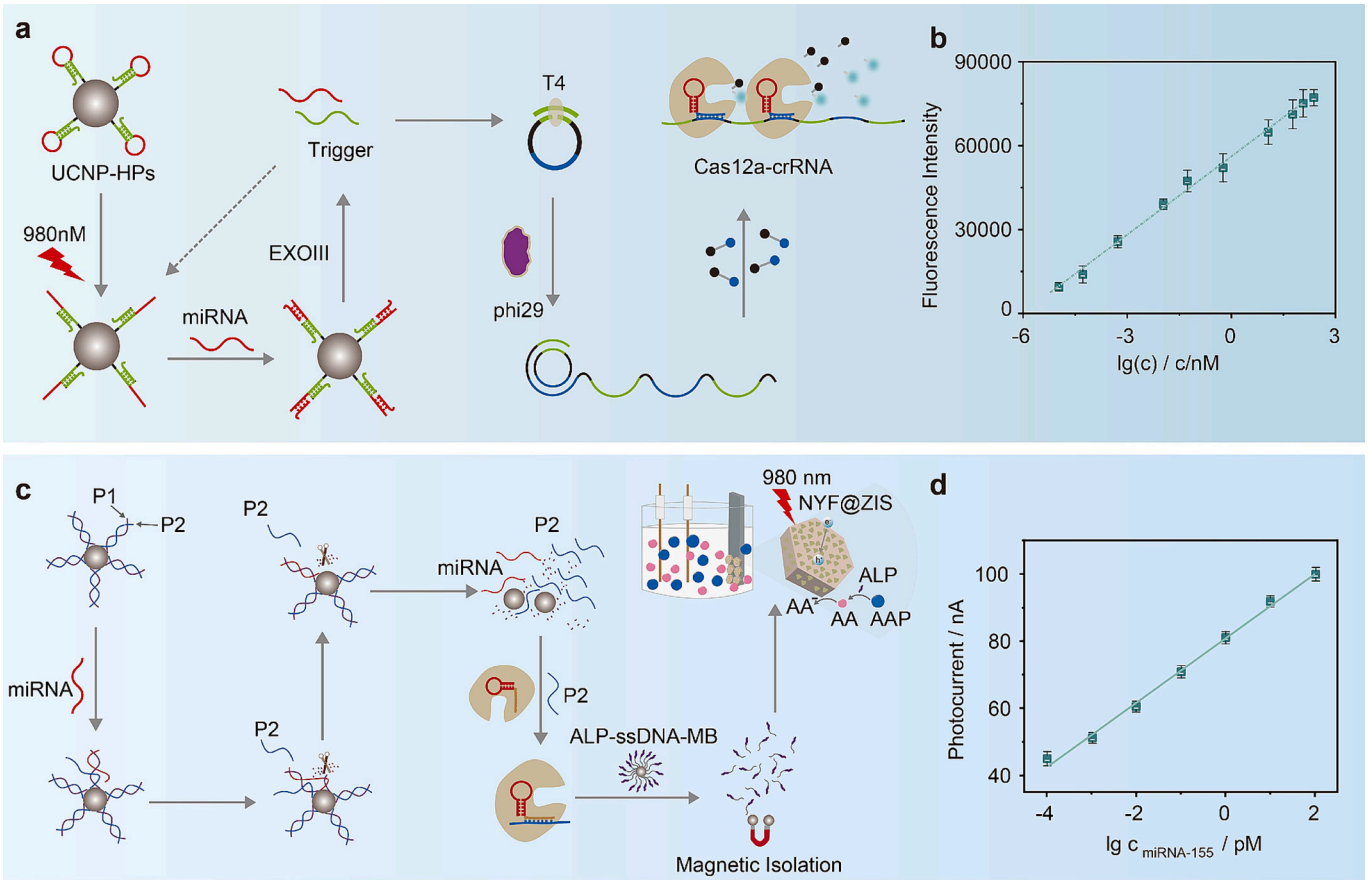

Fig. 4. UCNP-based CRISPR/Cas12a miRNA detection platforms. (**a**) Schematic illustration of miRNA detection method based on quenching DNA reporters and CRISPR/Cas12a-driven signal amplification coupled with SDA and RCA. (**b**) Fluorescence spectra corresponding to various concentrations of target miRNA-21, with a LOD of 6.01 fM Adapted with permission from Ref. [135]; Copyright 2023 Elsevier B.V. (**c**) Schematic illustration of miRNA detection method based on PEC and CRISPR/Cas12a-driven signal amplification coupled with 3D walking nanomotor. (**d**) Photocurrent for different concentrations of miRNA-155. Adapted with permission from Ref. [136]; Copyright 2024 Elsevier Inc. HP, a hairpin structure; EXOIII, EXOIII exonuclease; T4, T4 ligase; phi29, phi29 polymerase; P1, biotinylated ssDNA (the purple line); P2, biotinylated ssDNA (the blue line); ALP, alkaline phosphatase; AAP, L-ascorbic acid 2-phosphate trisodium salt; AA, ascorbic acid; ALP-ssDNA-MB, ALP-ssDNA-modified magnetic beads; NYF@ZIS, $NaYF_4$: Yb, Tm@$ZnIn_2S_4$. (For interpretation of the references to colour in this figure legend, the reader is referred to the web version of this article.)

The 3D walking nanomotor amplification strategy employs strand displacement, deoxyribonuclease reaction, and the conformational transition to enable DNA to navigate along a predetermined path. In this method, biotinylated ssDNA (P1) that recognizes miRNA strands, and biotinylated ssDNA (P2) that activates Cas12a are loaded onto magnetic beads. When the target miRNA is present, it displaces the P2 chain. T7 exonuclease then digests the P1 strand from the 5' to 3' end, releasing the miRNA from the magnetic beads and allowing it to be recycled, providing the first amplification step. The released P2 activates Cas12a, leading to the release of alkaline phosphatase (ALP) from ALP-ssDNA-modified magnetic beads, serving as the second amplification step. ALP catalyzes the hydrolysis of L-ascorbic acid 2-phosphate trisodium salt (AAP) to generate ascorbic acid (AA), which acts as an effective hole-trapping agent and significantly amplifies the photocurrent of NYF@ZIS with high sensitivity (Fig. 4c). The reporting system uses $NaYF_4$: Yb, Tm@$ZnIn_2S_4$ (NYF@ZIS) as an excellent photoelectronic material. NYF acts as an energy donor, emitting ultraviolet /visible light under near-infrared irradiation, while ZIS serves as an energy acceptor, absorbing the high-energy light to generate photocurrent. The presence of ascorbic acid further amplifies the photocurrent of NYF@ZIS. The integration of UCNPs and PEC methods allows for the conversion of high-energy light into photocurrent, significantly enhancing detection sensitivity with a LOD of 65.77 aM (Fig. 4d) [136].

4.2. Sandwich structure-based miRNA detection

Using a sandwich structure for miRNA detection offers a simple and effective strategy, typically consisting of three components: a reporter, a probe, and a target. When using UCNPs, the LOD can reach the femtomolar level [137,138]. Several studies have successfully integrated this sandwich structure with UCNPs for miRNA detection, where UCNPs serve various roles, including energy donors [138], reference standards [139], and reporters [137,140]. This approach not only simplifies the detection process but also has the potential to develop miRNA test strips for point-of-care applications. Importantly, it does not require amplification or enzyme assistance, making it suitable for complex biological environments.

UCNPs can transfer energy to receptors through FRET. These receptors may include organic dyes [141], quantum dots [142], nanogolds [143]. For example, in a self-assembling multimode lateral flow assay (LFA) for detecting miR-21 [138], the reporters consisted of core-shell Au-DTNB@Ag nanoparticles and UCNPs ($NaYF_4$: Yb^{3+}, Er^{3+}). Single-layer UCNPs were immobilized on the T-line of a nitrocellulose membrane (Fig. 5a). A biotin-modified ssDNA probe was positioned in the area containing the UCNPs, while the Au-DTNB@Ag nanoparticles were modified with sulfonyl-modified ssDNA, where 5,5-dithiobis-2-nitrobenzoic acid (DTNB) produced unique surface-enhanced Raman scattering (SERS) signals [144,145]. The ssDNA on Au-DTNB@Ag nanoparticles are complementary to the C-line probe (Fig. 5b). When a

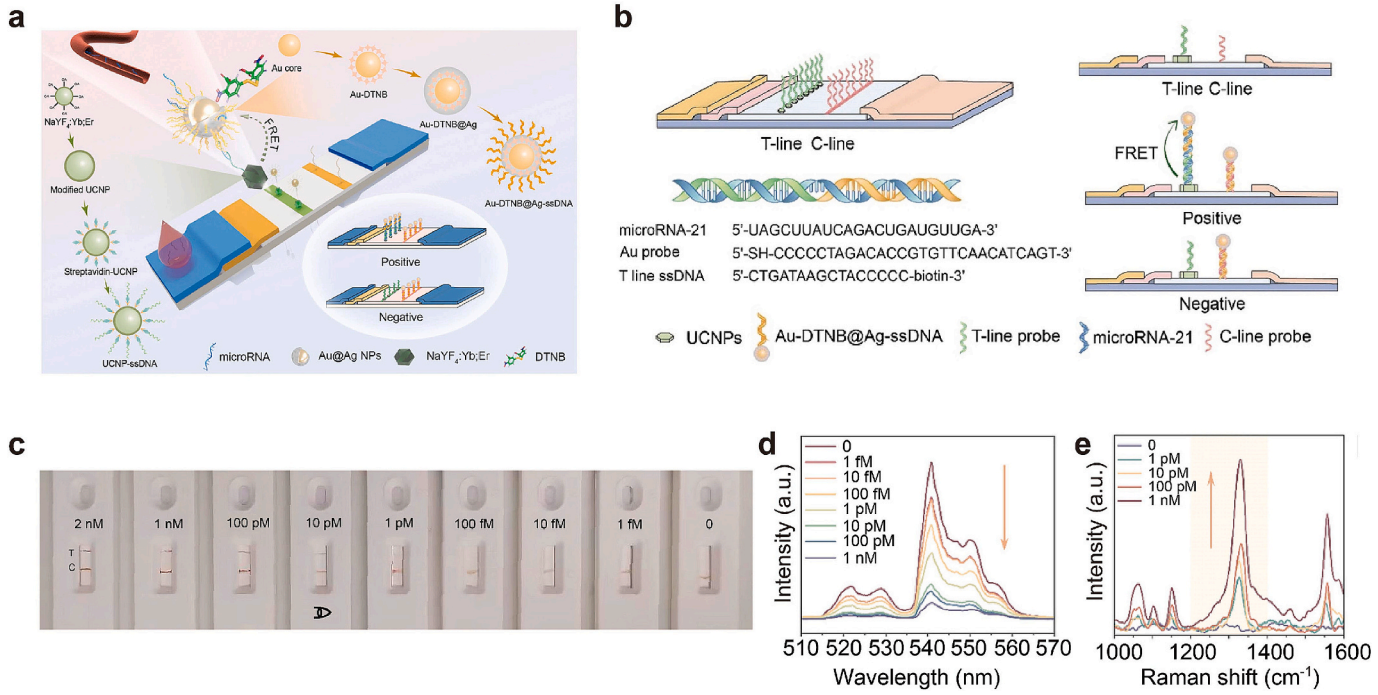

Fig. 5. Sandwich structure-based miRNA detection using LFA. (**a**) Synthetic route for the multimode LFA biosensor. (**b**) Principle of the multimode LFA biosensor designed for miRNA detection. (**c**) Colorimetric detection results of the LFA biosensor at various miR-21 concentrations. (**d**) Fluorescence emission spectra of the biosensor across different miR-21 concentrations. (**e**) SERS spectra of this biosensor at various miR-21 concentrations. Adapted with permission from Ref. [138]; Copyright 2024 Elsevier B.V.

sample is introduced to the sample pad, it migrates across the LFA strip through capillary action. The miRNA binds to the Au-DTNB@Ag-ssDNA probe via complementary base pairing, forming a composite structure that moves to the T-line. At the T-line, it interacts with the T-line probe, resulting in the aggregation of Au-DTNB@Ag nanoparticles and generating a visible orange band. Additionally, this aggregation leads to fluorescence quenching of the UCNPs, through the FRET process. The characteristic SERS peaks of DTNB can also be measured using Raman spectroscopy. Once the reaction at the T-line is complete, any excess Au-DTNB@Ag-ssDNA probes bind to the C-line probe, confirming successful

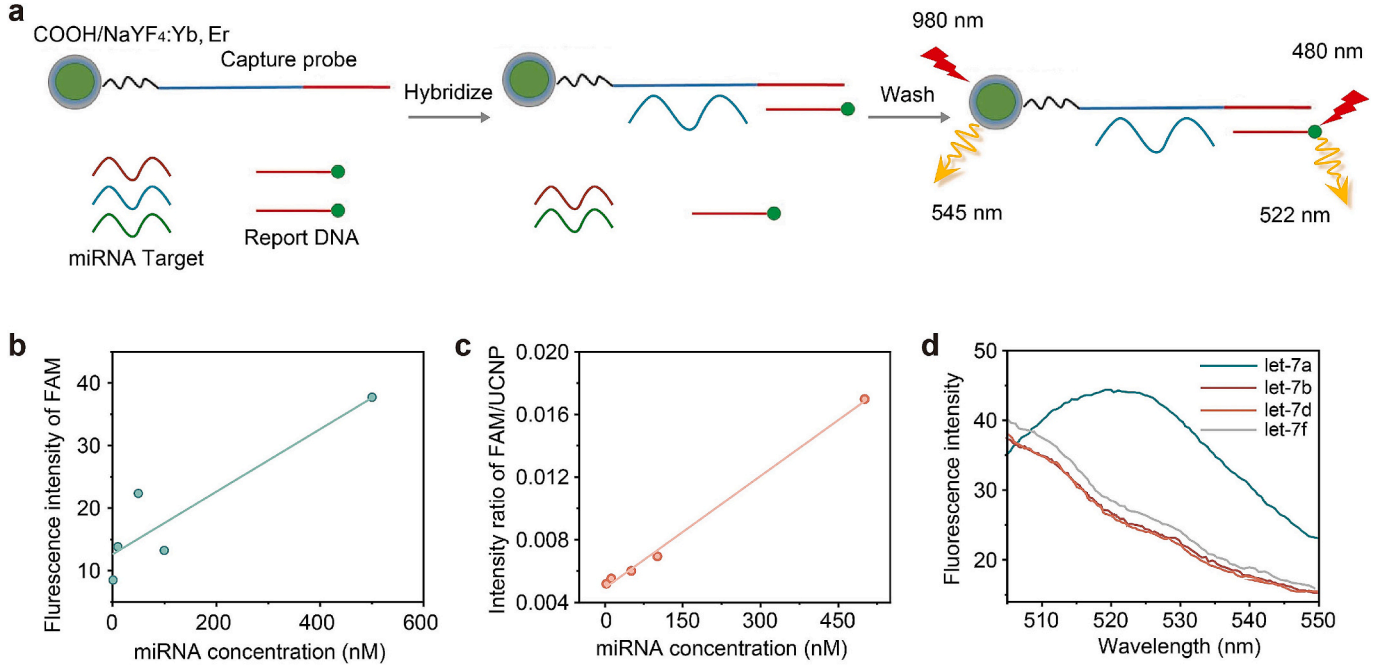

Fig. 6. Sandwich structure-based miRNA detection. (**a**) Schematic illustration of miRNAs detection using $NaYF_4$:Yb, Er UCNPs as a reference standard and base-stacking hybridization. (**b**) Linear relationships between let-7a concentration and the fluorescence intensity of FAM. (**c**) Linear relationships between let-7a concentration and the intensity ratios of FAM/UCNPs. (**d**) Fluorescence intensity at 480 nm of report DNA for let-7 family. Adapted with permission from Ref. [139]; Copyright 2016 Science China Press and Springer-Verlag Berlin Heidelberg.

assay execution. If the target analyte is absent, only the C-line will be visible. This multimode signal acquisition system addresses the limitations of false positives at low target concentrations that are common in LFA platforms. The sensitive fluorescence signal from UCNPs significantly enhances the overall sensitivity of the system. For example, the minimum colorimetric detection limit is 2 nM (Fig. 5c), the LOD for fluorescence detection is 1 fM (Fig. 5d) and the LOD for SERS is 1 pM (Fig. 5e).

UCNPs can also function as a reference to enhance the accuracy of sensing probes eliminating the need for complex calibration of emission intensity. As illustrated in Fig. 6a [139], the capture probe in this detection system consists of three segments: a poly(A) segment that acts as a spacer, a middle segment complementary to the target miRNA, and a 10-base segment complementary to the report DNA. This capture probe is covalently linked to UCNP ($NaYF_4$: Yb^{3+}, Er^{3+}) via the amino group on the probe and the carboxylic acid on UCNPs. When miRNA targets are present, they bind to the capture probe, allowing the FAM-labeled report DNA to attach as well. This miRNA binding is essential for stabilizing the report DNA through base stacking interactions, which are stronger than hydrogen bonds and vital for maintaining the integrity of the DNA double helix [146,147]. Without miRNA, the report DNA cannot bind stably to the probe. The principle of base stacking has been widely utilized in various studies [148,149]. Researchers noted a weak linear correlation between the fluorescence intensity of FAM and miRNA concentration (R^2 = 0.779) (Fig. 6b), but observed a strong linear relationship when using the fluorescence intensity ratio of FAM/UCNP (R^2 = 0.996) (Fig. 6c). This indicated that employing UCNP as a reference and utilizing the FAM/UCNP intensity ratio enhances the accuracy and reproducibility of miRNA detection, underscoring the critical role of UCNPs. Additionally, this system successfully differentiates miRNA let-7a from other members of the let-7 family, demonstrating its specificity (Fig. 6d).

Using UCNPs as reporters is a widely adopted strategy that can be divided into two approaches based on the detection principle: grasping [137] and dissociation [140]. In grasping-based detection, the target miRNA acts as a bridge between the reporter and the probe, primarily through complementary base pairing and base stacking hybridization [137]. For instance, poly (acrylic acid)-coated $NaYF_4$:Yb^{3+},Er^{3+} UCNPs, covalently functionalized with hairpin-structured DNA tracer probes, are used in a sandwich format. Biotin-modified hairpin capture probes are immobilized onto microtiter wells via streptavidin. When the target miRNA is present, it connects the UCNPs and tracer probes, facilitating

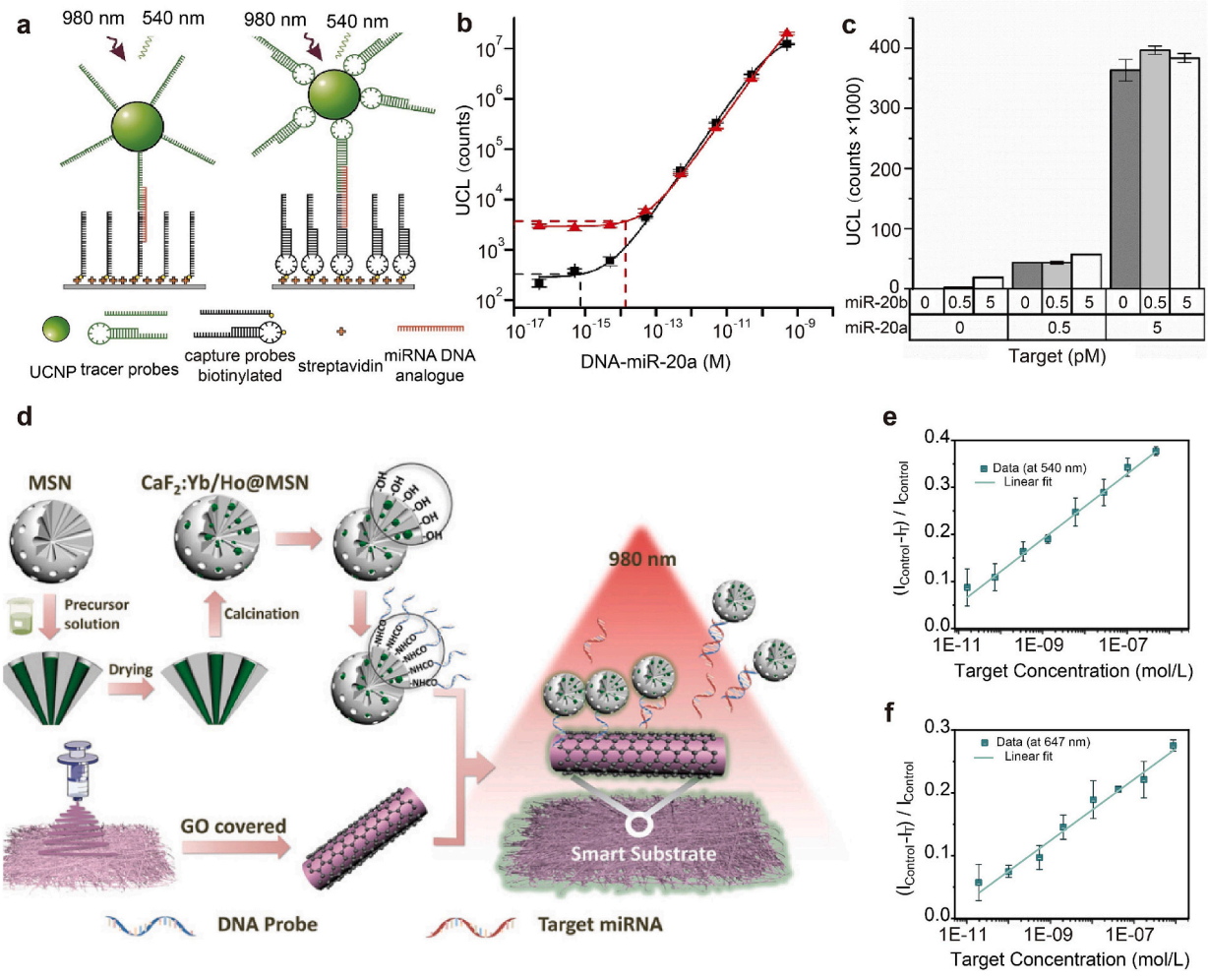

Fig. 7. Sandwich structure-based miRNA detection. (**a**) The sandwich structure of probes, miRNA, and UCNP with linear probes (left) or hairpin-structured probes (right). (**b**) The relationship between UCL and target concentration is shown for hairpin structured (black, squares) and linear probes (red, triangles). Dashed lines indicate the limits of detection, which are 0.73 fM for hairpin probes and 13 fM for linear probes. (**c**) UCL using hairpin structured probes to detect various combinations of complementary (DNA-miR-20a) and non-complementary (DNA-miR-20b) targets. Adapted with permission from Ref. [137]; Copyright 2019 The Royal Society of Chemistry. (**d**) Schematic illustration of the biosensing membrane synthesis (left) and the dissociation principle of miRNA detection (right). The linear relationship between the relative intensity of UCL, at (**e**) 540 nm and (**f**) 647 nm, and different miR-21 concentrations. Adapted with permission from Ref. [140]; Copyright 2024 Analysis & Sensing. MSN, mesoporous silica nanoparticles; GO, graphene oxide. (For interpretation of the references to colour in this figure legend, the reader is referred to the web version of this article.)

detection through changes in upconversion luminescence signals (Fig. 7a). This method achieved a detection limit of 0.73 fM (Fig. 7b) and could differentiate between miR-20 family members (Fig. 7c). The study demonstrated that UCNPs conjugated with hairpin probes exhibited stronger hybridization with target DNA, higher specificity, and more distinct UCL signals compared to linear probes, attributed to base stacking effect (Fig. 7a) [137].

In dissociation-based detection, the target miRNA destabilized the sandwich structure. For example, ssDNA probes-modified mesoporous silica nanoparticles (CaF_2:Yb/Ho@MSNs) act as reporters and attached to flexible polyurethane fibers coated with graphene oxide(GO) via π-π stacking interactions (Fig. 7d). GO strongly interacts with ssDNA via π-π stacking, but the adsorption of dsDNA onto GO is impeded by the shielding effect of the phosphate backbone [150,151]. When the target miRNA is present, it forms dsDNA with the probes through complementary base pairing, causing the MSNs to dissociate from polyurethane fibers. The method achieved a detection limit of 20 pM, with a dynamic range of 20 pM to 1 μM (Fig. 7e and Fig. 7f) [140].

4.3. Energy transfer-based miRNA detection

Luminescence resonance energy transfer (LRET) is a non-radiative energy transfer mechanism between donor and acceptor, widely used in biosensing and imaging applications. The detection efficacy is influenced by five main factors: the types of donors and acceptors, the donor-acceptor distance, dipole moment orientation, donor and acceptor concentration, and the detection environment. Donors with long luminescence lifetimes [152], such as UCNPs, are often preferred. Acceptors can include Cy series dyes (e.g. Cy3, Cy5) [153,154], inorganic nanomaterials (e.g. gold nanoparticles [155], graphene oxide [156]), black hole quenches (BHQ1, BHQ2, BHQ3) [157], and quantum dots [158]. The efficiency of energy transfer increases with greater overlap between the donor's emission spectrum and the acceptor's absorption spectrum [159]. Effective LRET typically occurs when the donor-acceptor distance is within 10 nm, necessitating a thin shell around UCNPs [160]. Dipole moments can be parallel, antiparallel, or perpendicular, with parallel orientation yielding the highest energy transfer efficiency [161]. Concentration plays a crucial role; high concentrations of donor-acceptor pairs can lead to aggregation and uncontrolled energy transfer, while low concentrations may diminish detection sensitivity [162]. Environmental factors such as pH, temperature, and ion strength, also affect LRET efficiency [163]. Common detection platform designs include hairpin, sandwich, and pyramid configurations. The following sections will discuss LRET-based miRNA detection using these structures.

LRET-based hairpin structures are often linked to black hole quenches family, a series of non-fluorescent molecules widely used in fluorescence detection systems for quenching purposes. The main BHQ series, BHQ1, BHQ2, BHQ3, differ primarily in their absorption spectrum ranges and pairing abilities with fluorescent dyes [164]. BHQ molecules lack intrinsic fluorescence and can efficiently quench fluorescence by converting absorbed energy into heat or through intramolecular vibration via non-radiative processes [165]. These enhance the signal-to-noise ratio and detection sensitivity.

Hairpin structures are common nucleic acid with self-complementary sequences that form stable secondary structures. In LRET-based systems, the hairpin is attached to a BHQ at one end and fixed to UCNPs on the other, positioning the BHQ close to the UCNPs and facilitating efficient LRET. As shown in Fig. 8a, hairpin-shaped carboxyl molecular beacons (MB) with a BHQ3 quencher were covalently grafted onto SiO_2@UCNP nanofibers [157]. The absorption range of BHQ3 (600–730 nm) overlaps with the red-light emission from UCNPs, effectively quenching the red emission at 660 nm following MB immobilization (Fig. 8b). Upon the introduction of target miRNA, complementary hybridization opens the hairpin structure, restoring red-light emission at

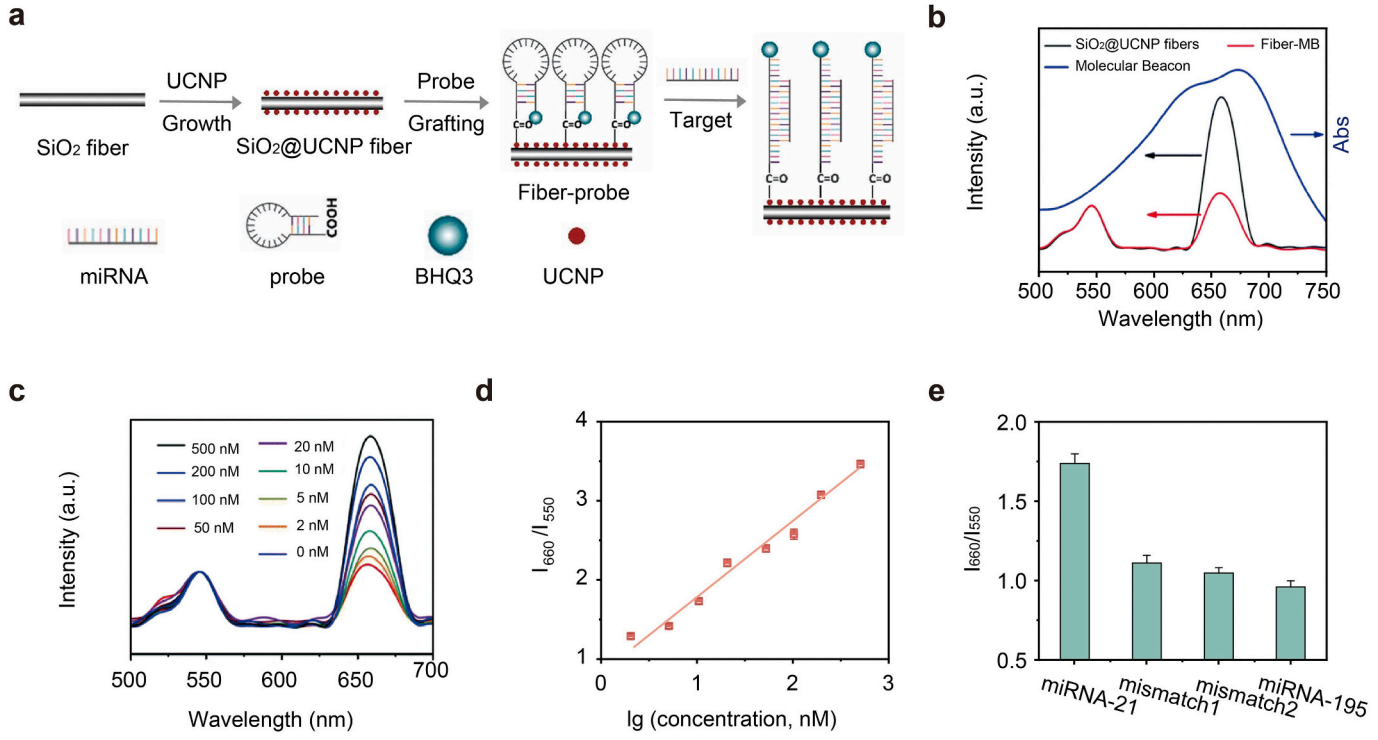

Fig. 8. LRET-based miRNA detection with a hairpin structure. (a) Schematic illustration of the LRET-based miRNA detection method utilizing hairpin structure. (b) Upconversion luminescence spectra of SiO_2@UCNP fibers before (black) and after (red) grafting the molecular beacon, alongside the absorption spectrum of the molecular beacons (green). (**c**) UCL of SiO_2@UCNP fibers at various concentrations of miRNA-21. (**d**) The intensity ratio I_{660}/I_{550} plotted against miRNA-21 concentration. (e) I_{660}/I_{550} ratio for SiO_2@UCNP fibers with miRNA-21, miRNA-21 with single base mismatch, miRNA-21 with three bases mismatches, and miRA-195. Adapted with permission from Ref. [157]; Copyright 2018 Royal Society of Chemistry. (For interpretation of the references to colour in this figure legend, the reader is referred to the web version of this article.)

660 nm and altering the intensity ratio I_{660}/I_{550} (Fig. 8c). This method achieved a LOD of 2 nM (Fig. 8d) and can differentiate single-base mismatches (Fig. 8e).

Combining UCNPs with quantum dots enhances the detection limit. In this design, UCNPs serve as the core, while mesoporous SiO_2 serves as shells to encase the UCNPs, with QDs (CsPbBr3) grown in situ within the mesopores, resulting in a composite fluorescent probe (MB-UCNP@SiO_2 + QDs) (Fig. 9a). This arrangement allows the multi-emission light from the UCNPs to re-excite the QDs through LRET. By fine-tuning the halogen doping ratio in the QDs, optimal spectral overlap at 531 nm is achieved (Fig. 9b). The probe features UCNP@SiO_2 + QDs and BHQ1 quenching groups positioned on either side of the molecular beacon. Upon binding to miRNA-155, the molecular beacon loop opens, displacing the BHQ1 quencher and restoring the fluorescence of UCNP@SiO_2 + QDs at 531 nm (Fig. 9c). This platform enables specific recognition and detection of miRNA-155 with a limit of 73.5 pM (Fig. 9d and Fig. 9e) [166].

The sensitivity of miRNA detection can be improved by creating a core-shell structure where UCNPs doped with emitting ions (Er^{3+}) are positioned near the surface to minimize the energy transfer distance (Fig. 10a). To facilitate the assembly of BHQ1 on the UCNP surface, phosphorylated and methylated tentacle DNAs (P-tDNA-M) were coated onto the UCNPs, enabling the capture of BHQ1-HP1 and forming a donor-acceptor pair (BHQ1-UCNPs). The absorption spectrum of BHQ1 closely overlaps with the UCNP emission at 543 nm (Fig. 10b). When target miRNA-21 is present, HP1 opens its loop, displacing BHQ1 from the UCNPs and restoring upconversion luminescence. As BHQ1-HP1 opens, it reveals the binding site for H2 in the BHQ1-HP1 sequence, allowing H2 to compete with miRNA for HP1, which further releasing miRNA and exposing additional BHQ1-HP1. This platform achieves highly sensitive detection of miRNA-21 with a detection limit of 75.3 fM (Fig. 10c) [167].

The hairpin structure, when paired with enzyme-catalyzed amplification, can achieve remarkable detection sensitivity. In a typical setup (Fig. 11a), the 8–17 DNAzyme BHQ1 is attached to $NaYF_4$: Yb, Er @ $NaYF_4$, forming energy donor-acceptor pairs (BHQ1-UCNPs). The target miR-21 displaces the aDNA (a DNA fragment partially paired with the capturing template), causing the released aDNA to open the 8–17 DNAzyme-BHQ1 and reveal the rA site. In the presence of Zn^{2+}, the rA site is cleaved, releasing miRNA, which then rebinds to the capturing template-aDNA, generating multiple aDNAs that form circles. This allows a small amount of miRNA to trigger the opening of numerous hairpin structures. This detection strategy has been validated in both cellular and mouse models. As the rA site is cleaved, BHQ1 is displaced from the UCNPs, restoring their luminescence. This method achieved a limit of detection of 31 fM (Fig. 11b and Fig. 11c) [24].

The key difference between the LRET-based sandwich structure and the previously described sandwich structure is the minimal distance required between the receptor on the reporter to the UCNPs. In the example shown in Fig. 12a, the receptor Cy3 is attached to the 3' end of the reporter, which aligns with capture 20a at the same end. This configuration reduces the distance between Cy3 and the UCNPs to just 2

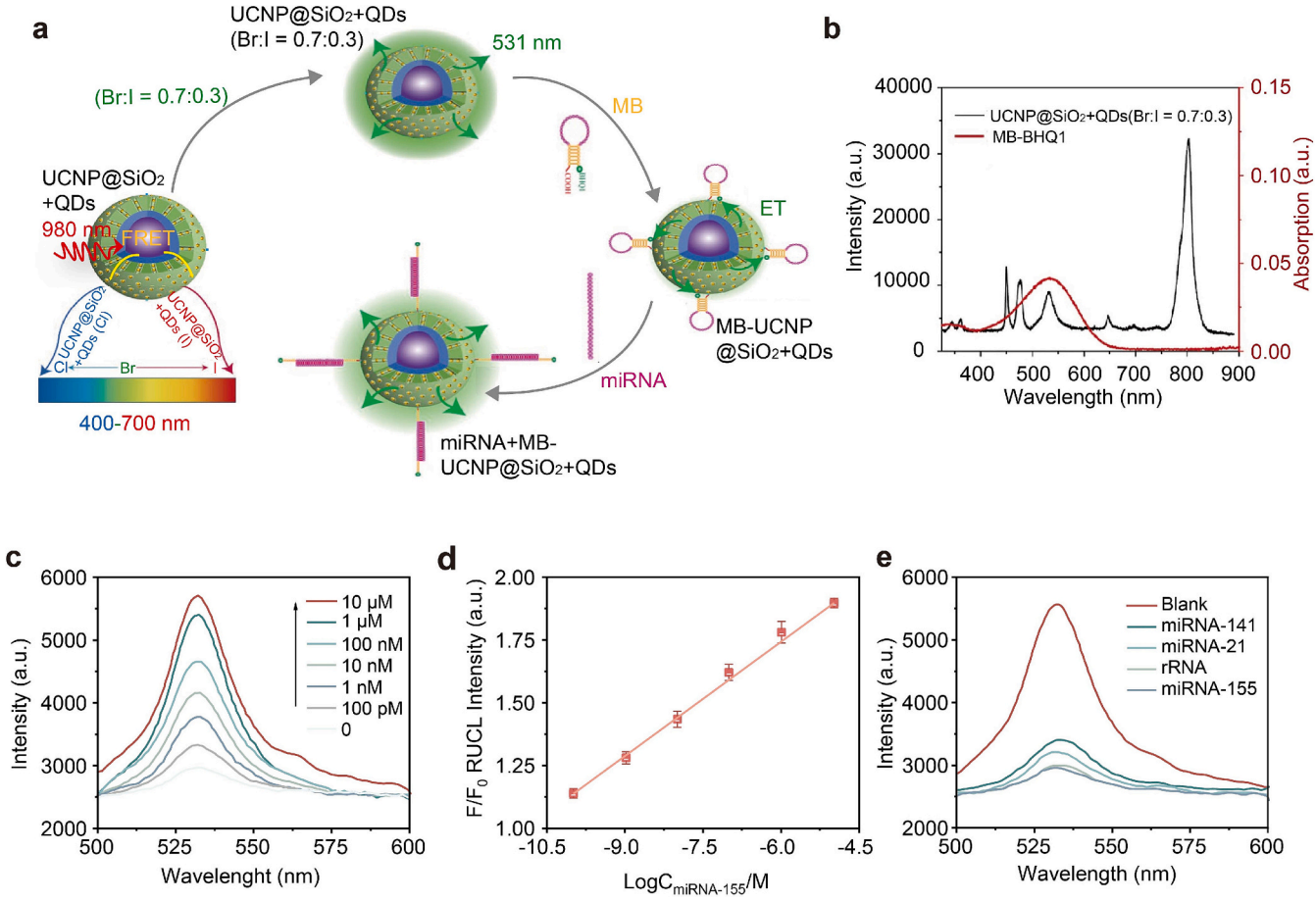

Fig. 9. LRET-based miRNA detection combined with QDs. (**a**) Schematic illustration of the miRNA detection method utilizing a hairpin structure combined UCNPs and QDs. (**b**) Fluorescence spectrum of UCNP@SiO_2 + QDs (Br: $I = 0.7{:}0.3$) alongside the absorption spectrum of MB-BHQ1. (**c**) UCL intensity of fluorescent probes of MB-UCNP@SiO_2 + QDs for various miRNA-155 concentrations. (**d**) The fluorescence intensity ratio plotted against miRNA-155 concentration. (**e**) UCL intensity of fluorescent probes of MB-UCNP@SiO_2 + QDs for detecting miRNAs with different base sequences. Adapted with permission from Ref. [166]; Copyright 2023 Springer Nature. QDs, quantum dots; MB, molecular beacons; BHQ1, black hole quench 1.

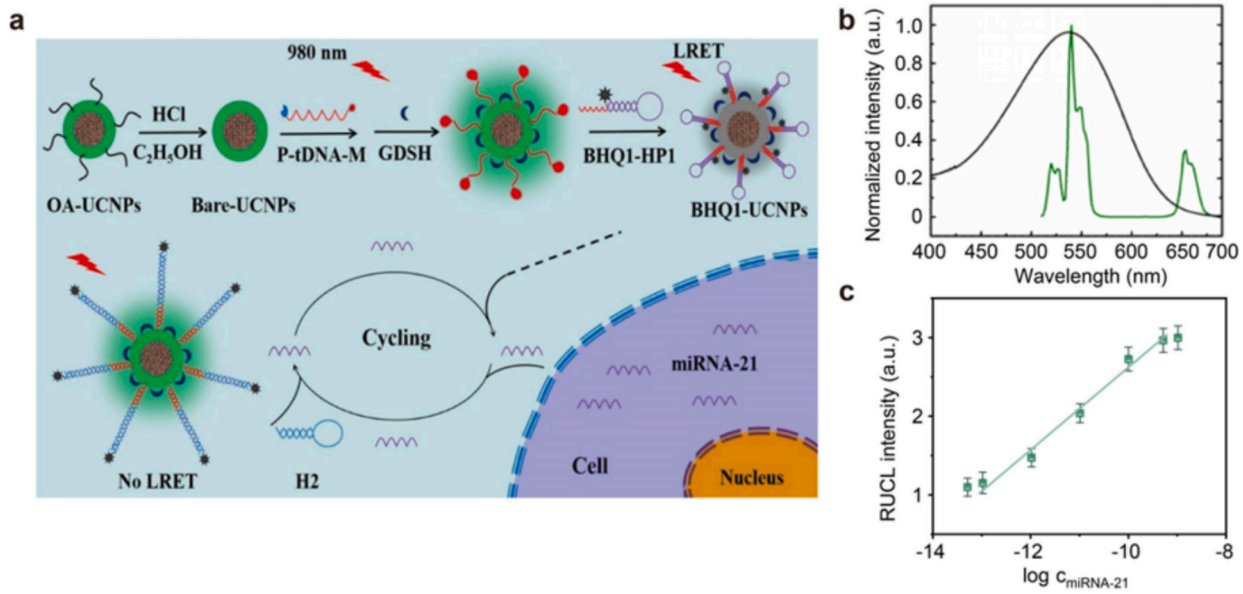

Fig. 10. LRET-based miRNA detection combined with CHA. (**a**) Schematic illustration for miRNA detection method utilizing hairpin structure combined with CHA. (**b**) Fluorescence spectra of UCNPs (green) and absorption spectra of BHQ1 (black). (**c**) The relative upconversion luminescence intensity (RUCL) as a function of the miRNA-21concentration. RUCL derived from ratio of upconversion luminescence intensity after incubating with miRNA over its original intensity. Adapted with permission from Ref. [167]; Copyright 2021 Elsevier B.V. P-tDNA-M, phosphorylated and methylated tentacle DNAs; BHQ1-HP1, capturing hairpin DNA labeled with BHQ1; H2, a hairpin DNA. (For interpretation of the references to colour in this figure legend, the reader is referred to the web version of this article.)

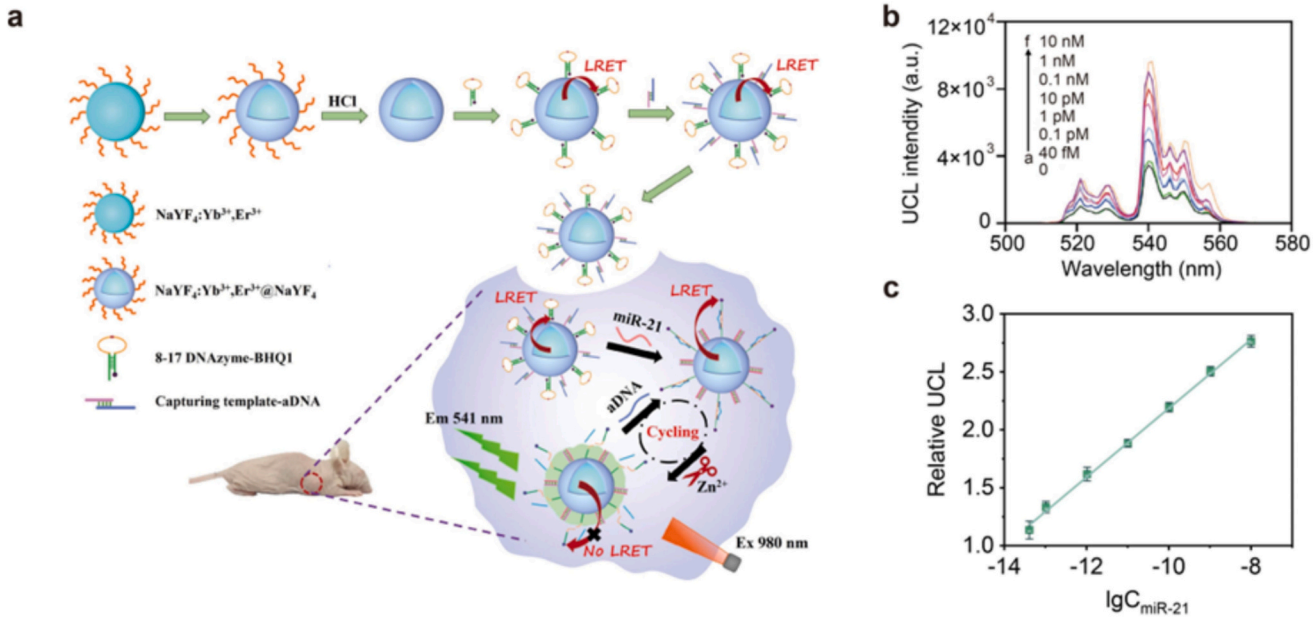

Fig. 11. LRET-based miRNA detection combined with enzyme-catalyzed amplification. (**a**) Schematic illustration if the miRNA detection method utilizing a hairpin structure coupled with enzyme-catalyzed amplification. (**b**) UCL intensity of UCNP probes at varying concentrations of miR-21. (**c**) The RUCL intensity as a function of the miRNA-21 concentration. Adapted with permission from Ref. [24]; Copyright 2022 Elsevier B.V.

nm thick layer of poly (sodium 4-styrene sulfonate). Additionally, Cy3 absorption spectrum aligns well with the green emission spectrum of UCNPs, facilitating LRET and generating fluorescence signals from Cy3. Since the region matching capture 20a consists of only eight bases, the absence of miRNA prevents stable binding due to inadequate base stacking forces. This system achieved a LOD of 4.5 fM (Fig. 12b) [168]. In contrast, Fig. 12c presents a different sandwich structure utilizing graphene quantum dots, which bind strongly to ssDNA through π-π stacking forces. When miRNA hybridizes with ssDNA on UCNPs to form dsDNA, the nucleotide bases become shielded by the phosphate backbone, resulting in the loss of binding for graphene quantum dots and their subsequent detachment from the UCNPs. This leads to reduction in photoluminescence emission signals at 550 nm and 650 nm, with the intensity negatively correlating with miRNA concentration (Fig. 12d) [169].

In the LRET-based pyramid structure, gold nanoparticles (AuNPs) and UCNPs are assembled into a pyramid configuration using DNA-driven self-assembly, ensuring close proximity between the donor and acceptor for effective energy transfer. The AuNPs act as receptor, exhibiting strong surface plasmonic resonance that efficiently absorbs

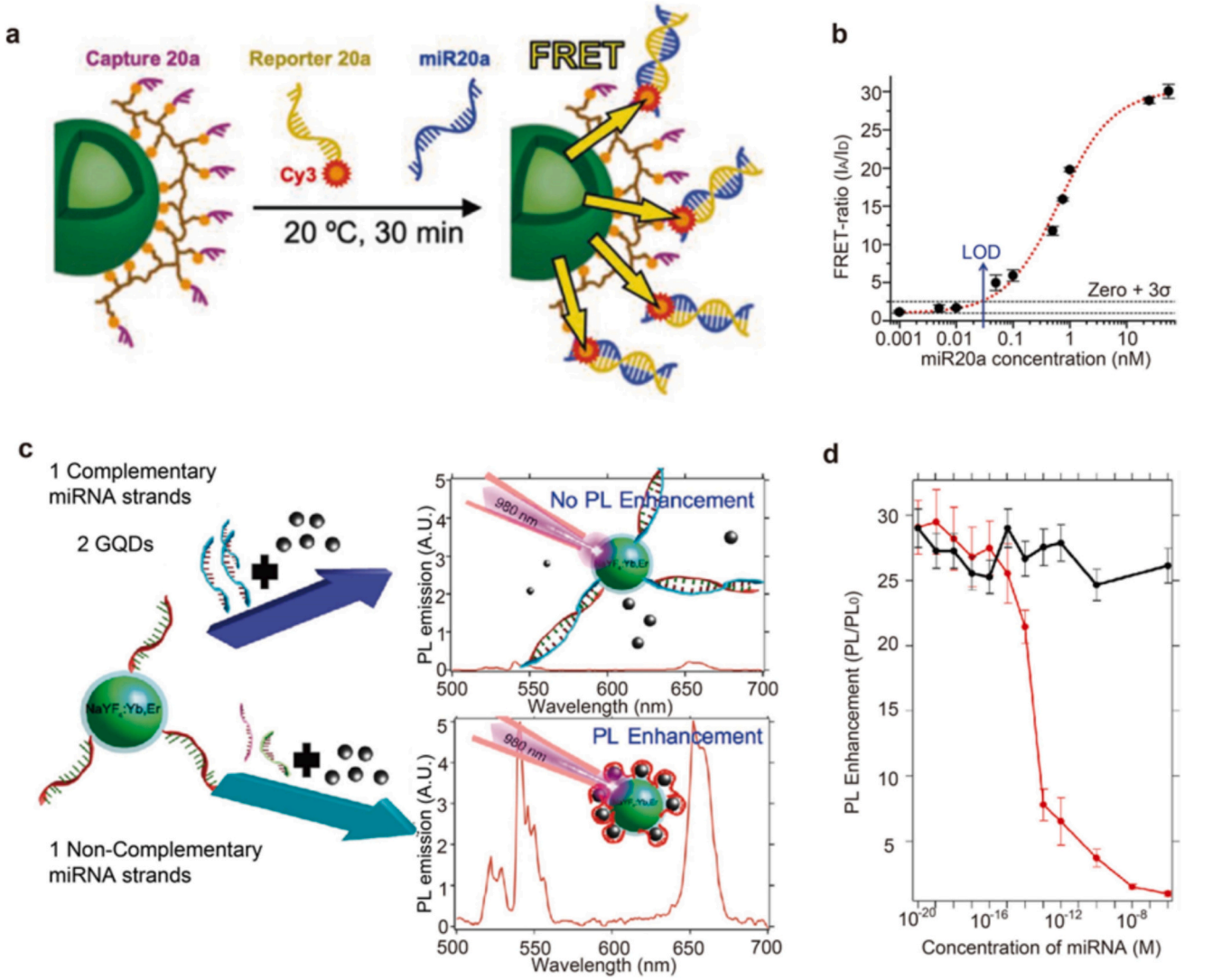

Fig. 12. LRET-based sandwich structure for miRNA detection. (**a**) Schematic illustration of a miRNA detection method using sandwich structure with a Cy3-reporter. (**b**) The FRET ratio between the acceptor (Cy3-DNA6) and donor (UC@PSS@DNA5) nanohybrid (λ_{exc} = 980 nm) at various concentration of miR-20a. Adapted with permission from Ref. [168]; Copyright 2022 Wiley-VCH GmbH. (**c**) Schematic illustration of a miRNA detection method based on sandwich structure through graphene quantum dot dissociation. (**d**) Graphs showing photoluminescence enhancement as a function of complementary miRNA concentration (red) compared to the enhancement observed with noncomplementary miRNA sequences (black). Adapted with permission from Ref. [169]; Copyright 2016 American Chemical Society. GOQs, graphene quantum dots; PL, photoluminescence. (For interpretation of the references to colour in this figure legend, the reader is referred to the web version of this article.)

and quenches the luminescent energy from the UCNPs. This precise arrangement allows the pyramid structure to demonstrate chiral optical activity, producing plasmonic circular dichroism (CD) signals while simultaneously quenching UCNP luminescence via LRET (Fig. 13a). When miRNA is present, it disrupts the pyramid structure, leading to the separation of AuNPs from UCNPs and diminishing the LRET effect, which restores the luminescent signal of UCNPs (Fig. 13b). The CD signal is also lost in this process (Fig. 13c). This method achieves a limit of detection of 0.03 fM, with the dual signals enhancing detection accuracy (Fig. 13d) [170].

4.4. ICP-based miRNA detection

Inductively coupled plasma mass spectroscopy (ICP-MS) is a powerful analytical technique for the precise detecting and quantification of multiple elements. While traditional ICP-MS is typically used for liquid samples, laser ablation-induced coupled plasma mass spectrometry (LA-ICP-MS) is effective for solid samples, making it valuable in biomedical analysis, food safety, and environmental monitoring. Combining LA-ICP-MS with lanthanide-labeled DNA probes offers a robust method for detecting miRNAs. As shown in Fig. 14a, this approach enhances DNA probe labeling inspired by Northern blot technique. Conventional Northern blot tags include radioactive tags (e.g. ^{32}P, ^{35}S, and ^{3}H) and non-radioactive tags (e.g. digoxin, biotin, and fluorescent dyes). In this setup (Fig. 14a), various lanthanide elements, such as thulium (Tm), terbium (Tb), holmium (Ho), or praseodymium (Pr), are used to label DNA probes, enabling the simultaneous detection of multiple miRNAs. Compared to ^{32}P tag, lanthanide labels provide a higher signal-to-noise ratio and sensitivity (Fig. 14b) [171]. However, this method requires miRNA levels above 0.1 ng for detection and can be time-consuming.

To enhance the sensitivity of ICP-MS-based miRNA detection, enzyme amplification can be integrated, utilizing enzyme like the Duplex-Specific Nuclease (DSN). DSN selectively digests DNA in DNA-RNA hybrids or dsDNA, leaving RNA and ssDNA intact. As shown in Fig. 14c, DNA probes labeled with various lanthanide elements are

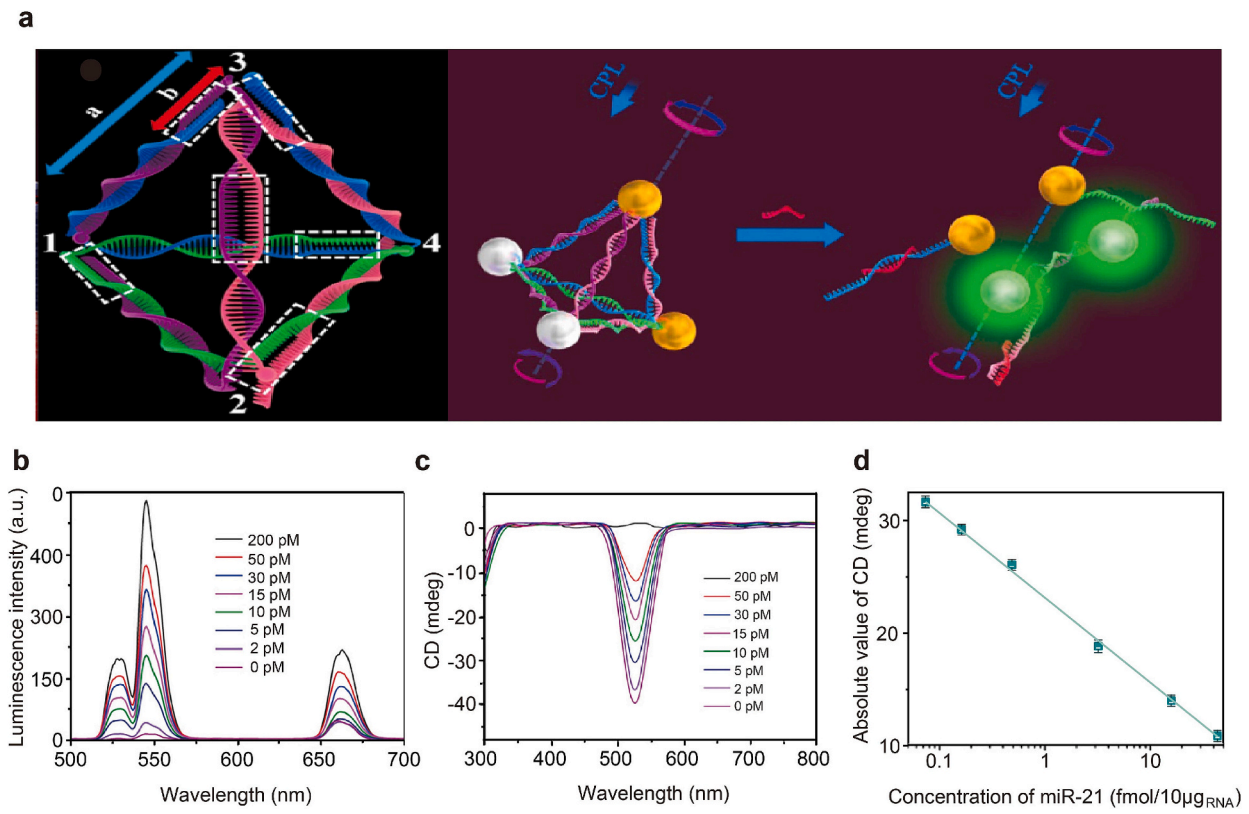

Fig. 13. LRET-based pyramid structure for miRNA detection. (**a**) Schematic illustration of the miRNA detection method utilizing a pyramid structure. (**b**) The UCL intensity of UCNPs responsive to various miR-21 concentrations. (**c**) The CD signal from the pyramid configurate of AuNPs and UCNPs at varying miR-21 concentrations. (**d**) The linear relationship between the CD value and concentration of miR-21. Adapted with permission from Ref. [170]; Copyright 2015 American Chemical Society.

immobilized on streptavidin-coated magnetic microparticles (MMP). When the target miRNA forms a heteroduplex with a DNA probe, DSN cleaves the DNA strand in the duplex. This cleavage releases the target miRNA and DSN, allowing the miRNA to hybridize with additional probes, which facilitates amplification. The intensity of the corresponding lanthanide elements in the supernatant is then quantified using ICP-MS (Fig. 14d) [172].

However, enzymes like DSN are sensitive to complex environments such as pH, temperature, and proteases, which may limit their effectiveness in plasma or other bodily fluid samples. To overcome these challenges, DNAzymes, known for their stability and similar catalytic function, have gained attention. Unlike proteins, DNAzyme retain their activity in environments lacking specialized DNases. A study introduced multi-component nuclear acid enzymes (MNAzymes), a derivative of DNAzymes, combined with ICP to detect miRNAs. In this approach, MNAzymes, which consist of partzyme A and B, only assemble their catalytic structure in the presence of target miRNAs. Once activated, the MNAzymes cleave specific DNA probes, releasing lanthanide tags. These enzymes then continue cleave complementary probes, allowing the miRNA concentration to be measured using ICP-MS (Fig. 14e). This method achieved detection limits for three miRNAs in the range of 11–20 pM (Fig. 14f) [173].

5. Challenges

Although significant progress has been made in developing lanthanide-doped nanoparticle-based strategies for miRNA detection, translating laboratory findings into clinical practices remains challenging. Several issues must be addressed, including variations in sample processing, patient variability, and the need for improved sensor robustness and adaptability.

5.1. Variations caused by sample processing

Although research indicates that miRNA are stable in bodily fluids [174], inconsistent results across laboratories may arise from differences in sample handling protocols [175]. Factors such as the type of sample (plasma or whole blood), storage temperature, physical disturbance and freeze-thaw cycles can all affect miRNA content [176]. To ensure more reliable results, it is crucial to establish standardized sample collection and processing protocols to minimize degradation of miRNA. Creating a centralized miRNA database with standardized procedures could significantly enhance the potential of miRNA as a biomarker for clinical disease diagnosis.

5.2. Patient variability

Genetic background, disease progression, dietary differences contribute to variations in pH, salt content, and enzyme concentration of body fluids, complicating sensor accuracy among individuals. Expanding the sample size is essential to improve sensor robustness. Consortiums and collaboration among multiple research centers, both national and internationally, is vital to enhance sensor reliability and clinical applicability. Additionally, advanced computational models using machine learning could be used address biological variability and improve sensor adaptability. Implementing these strategies alongside standardized sample collection and processing methods, would greatly enhance sensor reliability and clinical applicability.

6. Potential applications and perspectives

Lanthanides show significant promise for miRNA detection due to their unique physical and chemical properties. Lanthanide-doped

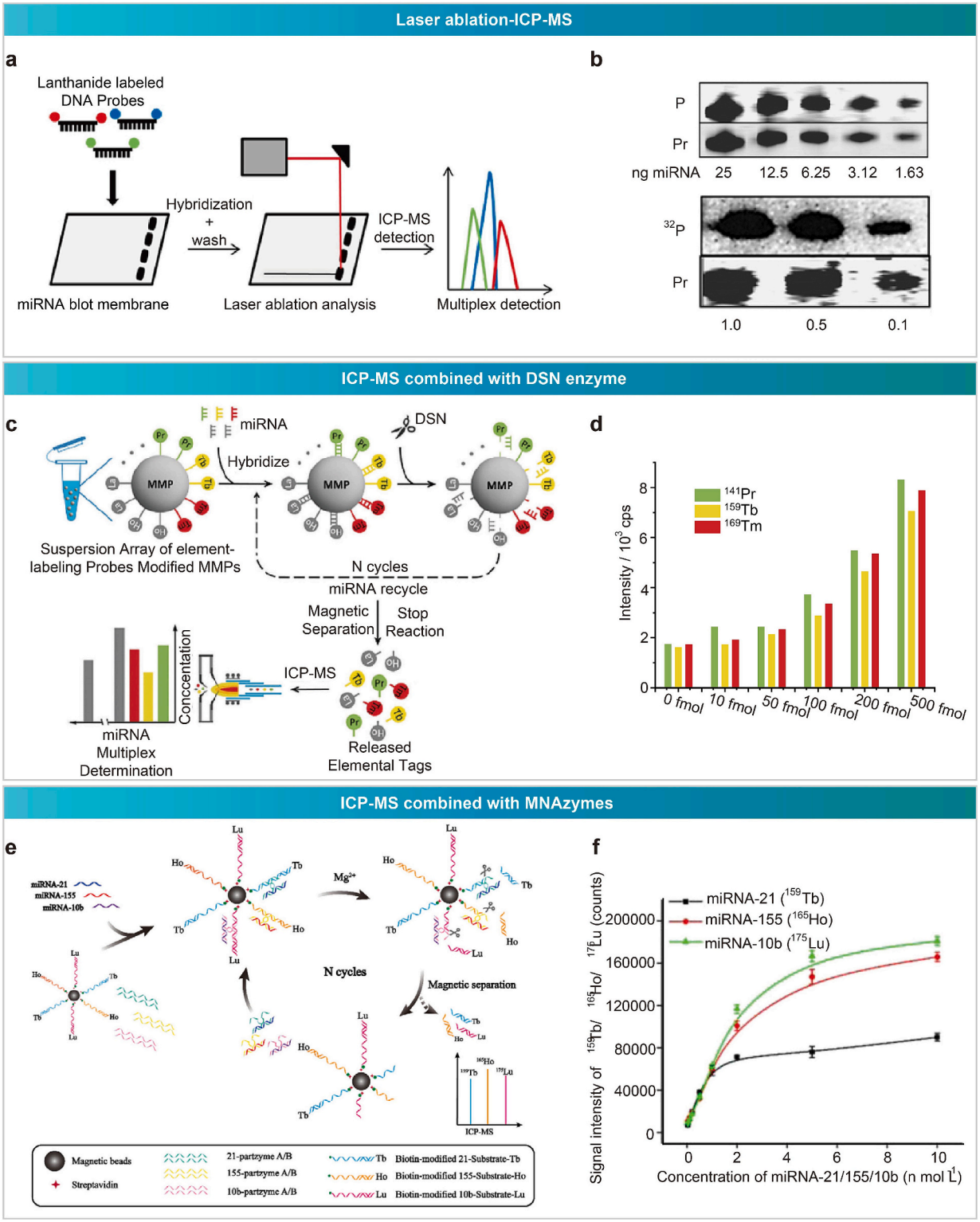

Fig. 14. ICP-based miRNA detection. (**a**) Illustration of miRNAs subjected to Northern blotted and incubated with lanthanide-labeled DNA probes. Following hybridization and washing, the membrane was analyzed by LA-ICP-MS. (**b**) LA-ICP-MS images displaying different miRNA concentrations based on the P (phosphorus) and Pr (praseodymium) signals, as well as autoradiography (^{32}P) of the 3 lowest concentrations of ath-miR160. Reproduced with permission from Ref. [171]; Copyright 2014 American Chemical Society. (**c**) Schematic illustration of the miRNA detection method using ICP-MS combined with DSN enzyme. (**d**) ICP-MS results showing the concentrations of three miRNAs analyzed simultaneously. Reproduced with permission from Ref. [172]; Copyright 2016 Royal Society of Chemistry. (**e**) Schematic illustration of the miRNA detection method using ICP-MS combined with MNAzymes. (**f**) The correlation between ICP-MS signals and the three miRNAs. Reproduced with permission Ref. [173]; Copyright 2021 American Chemical Society. ICP-MS, inductively coupled plasma mass spectroscopy; MMP, streptavidin-coated magnetic microparticles; DSN, duplex-specific nuclease; MNAzymes, multi-component nuclear acid enzymes.

nanoprobes have great potential for early disease diagnosis, as well as applications in forensics and disease prognosis.

6.1. Forensic evidence

Lanthanide-doped probes for miRNA have promising applications in forensic science for identifying the sources of bodily fluid, estimating the Post Mortem Interval (PMI), and determining causes of death. Different body fluids exhibit distinct miRNA profiles, enabling fluid sources inference based on miRNA types. For example, seven specific miRNAs (miR-144-3p, miR-451a-5p, miR-888-5p, miR-891a-5p, miR-203a-3p, miR-223-3p, and miR-1260b) have been identified that can differentiate between venous blood, saliva, semen, and vaginal secretions [14]. Additionally, mathematical models using miRNA have been developed to accurately estimate PMI [177]. Changes in miRNA expression profiles under different disease conditions can also provide insights into the cause of death. For example, in cases of myocardial infarction, miR-208 is upregulated while miR-1 and miR-133a are downregulated compared to healthy individuals [178]. Exposure to environmental factors, such as persistent organic pollutants, heavy metals, air pollution or toxins, can also alters miRNA expression patterns [12,13], potentially indicating whether death was duct to poisoning.

6.2. Disease prognosis

miRNAs are emerging as significant prognostic markers in disease such as breast cancer, T cell-acute lymphoblastic leukemia, prostate cancer, epithelial ovarian cancer [9,10]. In breast cancer patients, high level of hsa-miR-7 in plasma correlates with poor response to tamoxifen, reducing progression-free and overall survival. Elevated level of miR-21 levels are linked to trastuzumab resistance, while miR-34a is associated with chemotherapy resistance [11]. These miRNA signatures can aid clinicians in tailoring treatment plans to individual patients, aligning with the tread towards personalized therapy in clinical practice. As timely and accurate treatments become increasingly important, the development of advanced miRNA detection tools appears highly promising.

While the use of lanthanide-doped nanoprobes for miRNA detection is still in its early stages, ongoing advancements across various disciplines continue to improve the properties of these hybrids. Their exceptional performance shows potential for overcoming current challenges in miRNA detection, including high costs, complex procedures, and reliance on specialized instruments. Moving forward, interdisciplinary collaboration, enhanced detection strategies, larger validation sample sizes, and the integration of technologies like machine learning and big data in probe development, will drive progress in this area. We are optimistic that the development of simple, rapid, cost-effective, highly sensitive and specific lanthanide-doped nanoprobes will bridge laboratory findings with clinical practice, ultimately improve healthcare efficiency.

Declaration of competing interest

The authors declare that they have no known competing financial interests or personal relationships that could have appeared to influence the work reported in this paper.

Acknowledgements

The authors would like to acknowledge the UTS Chancellor's Research Fellowship Program (G.B., PRO23-17800), the Dust Diseases Board (G.B., PRO23-16473), the Tour De Cure grant (G.B., RSP-056-2025), and the National Natural Science Foundation of China (Y.L., Grant 12004232).

Data availability

No data was used for the research described in the article.

References

[1] M. Drobna-ledzińska, N. Makowska-Malak, R. Jaksik, P. Dbek, M. Witt, M. Dawidowska, Sci. Rep. 12 (2022) 6297.
[2] R.C. Friedman, K.K.-H. Farh, C.B. Burge, D.P. Bartel, Genome Res. 19 (2009) 92–105.
[3] M. Ha, V.N. Kim, Nat. Rev. Mol. Cell Biol. 15 (2014) 509–524.
[4] X. Chen, Y. Ba, L. Ma, X. Cai, Y. Yin, K. Wang, J. Guo, Y. Zhang, J. Chen, X. Guo, Q. Li, X. Li, W. Wang, Y. Zhang, J. Wang, X. Jiang, Y. Xiang, C. Xu, P. Zheng, J. Zhang, R. Li, H. Zhang, X. Shang, T. Gong, G. Ning, J. Wang, K. Zen, J. Zhang, C.-Y. Zhang, Cell Res. 18 (2008) 997–1006.
[5] R.C. Lee, R.L. Feinbaum, V.R. Ambros, Cell 75 (1993) 843–854.
[6] C. Lawrie, Br. J. Haematol. 141 (2010) 672–675.
[7] G.A.D. Metcalf, Oncogene 43 (2024) 2135–2142.
[8] P.S. Mitchell, R.K. Parkin, E.M. Kroh, B.R. Fritz, S.K. Wyman, E.L. Pogosova-Agadjanyan, A. Peterson, J. Noteboom, K.C. O'Briant, A. Allen, National Acad. Sci. 105 (2008) 10513–10518.
[9] S. Sabarimurugan, C. Kumarasamy, M.R. Madhav, S. Samiappan, R. Jayaraj, Cancer Manag. Res. 12 (2020) 819–839.
[10] S. Rana, G. Valbuena, E. Curry, C. Bevan, H. Keun, Br. J. Cancer 126 (2022) 502–513.
[11] E. Zografos, F. Zagouri, D. Kalapanida, R. Zakopoulou, A. Kyriazoglou, K. Apostolidou, M. Gazouli, M.A. Dimopoulos, Oncotarget 10 (2019) 7156–7178.
[12] J. Krauskopf, T.M. de Kok, D.G. Hebels, I.A. Bergdahl, A. Johansson, F. Spaeth, H. Kiviranta, P. Rantakokko, S.A. Kyrtopoulos, J.C. Kleinjans, Sci. Rep. 7 (2017) 9262.
[13] L. Hou, D. Wang, A. Baccarelli, Mutat. Res./Fundam. Mol. Mech. Mutagen. 714 (2011) 105–112.
[14] S. Fujimoto, S. Manabe, C. Morimoto, M. Ozeki, Y. Hamano, E. Hirai, H. Kotani, K. Tamaki, Sci. Rep. 9 (2019) 14332.
[15] R.R. Shi, V.L.V. Chiang, BioTechniques 39 (2005) 519–525.
[16] P.D.R. Cirillo, K. Margiotti, A. Mesoraca, C. Giorlandino, BMC Res. Notes 13 (2020) 351.
[17] C.M. Hindson, J.R. Chevillet, H.A. Briggs, E.N. Gallichotte, M. Tewari, Nat. Methods 10 (2013) 1003–1005.
[18] T. Gunel, M.K. Hosseini, E. Gumusoglu, H.I. Kisakesen, A. Benian, K. Aydinli, Placenta 52 (2017) 77–85.
[19] J.C. Alwine, D.J. Kemp, G.R. Stark, Proc. Natl. Acad. Sci. 74 (1977) 5350–5354.
[20] J. Ye, M. Xu, X. Tian, S. Cai, S. Zeng, J. Pharm. Anal. 9 (2019) 217–226.
[21] T. Chen, J. Yang, Y. Tang, X. Fan, W. Zhou, B. Jiang, D. Wang, Anal. Chim. Acta 1289 (2024) 342187.
[22] L. Li, K. Tan, Y. Bai, J. Chen, R. Dong, Z. Li, J. Wang, Anal. Chem. 96 (2024) 10274–10282.
[23] W. Wang, T. Kong, D. Zhang, J. Zhang, G. Cheng, Anal. Chem. 87 (2015) 10822–10829.
[24] Y. Zhang, D. Luo, Y. Zhang, Q.-H. Zhang, Q.-Y. Ji, S.-K. Zhou, S. Huang, L.-L. Li, F. Lu, W.-F. Yao, Chem. Eng. J. 454 (2023) 140489.
[25] G. Bao, R. Deng, D. Jin, X. Liu, Nat. Rev. Mater. 10 (2025) 28–43.
[26] Y. Luo, Z. Chen, S. Wen, Q. Han, L. Fu, L. Yan, D. Jin, J.C.G. Bunzli, G. Bao, Coord. Chem. Rev. 469 (2022) 214653.
[27] M. Xiang, Y. Jiang, J. Zhou, G. Bao, X. Luo, L. Zhang, D. Jin, Y. Xian, C. Zhang, Nano Today 54 (2024) 102110.
[28] Y. Luo, Q. Liu, P. He, L. Li, Z. Zhang, X. Li, G. Bao, K.L. Wong, P.A. Tanner, L. Jiang, Adv. Sci. 10 (2023) 2303235.
[29] G. Bao, D. Jin, Nat. Photonics 13 (2019) 304–305.
[30] G. Bao, S. Wen, G. Lin, J. Yuan, J. Lin, K.-L. Wong, J.-C.G. Bünzli, D. Jin, Coord. Chem. Rev. 429 (2021) 213642.
[31] Y. Zhu, X. Luo, Z. Yu, S. Wen, G. Bao, L. Zhang, C. Zhang, Y. Xian, Acta Biomater. 170 (2023) 532–542.
[32] G. Bao, S. Wen, W. Wang, J. Zhou, S. Zha, Y. Liu, K.-L. Wong, D. Jin, Nano Lett. 21 (2021) 9862–9868.
[33] S. Han, Z. Yi, J. Zhang, Q. Gu, L. Liang, X. Qin, J. Xu, Y. Wu, H. Xu, A. Rao, X. Liu, Nat. Commun. 12 (2021) 3704.
[34] D.E. McCoy, T. Feo, T.A. Harvey, R.O. Prum, Nat. Commun. 9 (2018) 1.
[35] Y. Liu, L. Ning, Y. Luo, Y. Huang, Z. He, H. Ma, Y. Zhao, J. Zhang, D. Liu, L. Fu, S. J. Langford, P.A. Gale, Y. Luo, G. Bao, Nano Lett. 24 (2024) 12486–12492.
[36] M.L. Aulsebrook, B. Graham, M.R. Grace, K.L. Tuck, Coord. Chem. Rev. 375 (2018) 191–220.
[37] Y. Zhang, Y. Cao, Y. Liu, Y. Yang, M. Chen, H. Gao, L. Lin, X. Chen, Nano Res. 16 (2023) 11250–11258.
[38] X. Song, M. Li, S. Ni, K. Yang, S. Li, R. Li, W. Zheng, D. Tu, X. Chen, H. Yang, Nano Lett. 23 (2023) 1878–1887.
[39] M.R. Winnett, P. Mini, M.R. Grace, K.L. Tuck, Inorg. Chem. 59 (2020) 118–127.
[40] G. Bao, J. Lumin. 228 (2020) 117622.
[41] B. Wightman, I. Ha, G. Ruvkun, Cell 75 (1993) 855–862.
[42] V. Ambros, B. Bartel, D.P. Bartel, C.B. Burge, T. Tuschl, RNA 9 (2003) 277–279.
[43] V. Ambros, Nature 431 (2004) 350–355.
[44] B.J. Reinhart, E.G. Weinstein, M.W. Rhoades, B. Bartel, D.P. Bartel, Genes Dev. 16 (2002) 1616–1626.
[45] B.R. Cullen, Nat. Genet. 38 (2006) S25–S30.

[46] K. Ana, B. Maria, G.J. Sam, Nucleic Acids Res. 47 (2018) D155–D162.
[47] Y. Lee, C. Ahn, J. Han, H. Choi, J. Kim, J. Yim, J. Lee, P. Provost, O. Rådmark, S. Kim, Nature 425 (2003) 415–419.
[48] E. Lund, S. Guttinger, A. Calado, J.E. Dahlberg, U. Kutay, Science 303 (2004) 95–98.
[49] V.N. Kim, J. Han, M.C. Siomi, Nat. Rev. Mol. Cell Biol. 10 (2009) 126–139.
[50] D.P. Bartel, Cell 136 (2009) 215–233.
[51] M.P. Gantier, C.E. McCoy, I. Rusinova, D. Saulep, D. Wang, D. Xu, A.T. Irving, M. A. Behlke, P.J. Hertzog, F. Mackay, Nucleic Acids Res. 39 (2011) 5692–5703.
[52] D.L. Michell, K.C. Vickers, Biochimica et Biophysica Acta (BBA)-Molecular and Cell Biology of Lipids 1861, 2016, pp. 2069–2074.
[53] A.A. Petkevich, A.A. Abramov, V.I. Pospelov, N.A. Malinina, E.I. Kuhareva, N. V. Mazurchik, O.I. Tarasova, Oncotarget 12 (2021) 1697.
[54] S. Jonas, E. Izaurralde, Nat. Rev. Genet. 16 (2015) 421–433.
[55] C. Kinoshita, Y. Okamoto, K. Aoyama, T. Nakaki, Clocks & Sleep 2 (2020) 282–307.
[56] L. Zhou, C. Miller, L.J. Miraglia, A. Romero, L.S. Mure, S. Panda, S.A. Kay, Proc. Natl. Acad. Sci. 118 (2021) e2020454118.
[57] H. Tai-You, Immune Netw. 11 (2011) 135–154.
[58] H.E. Kinser, Z. Pincus, Hum. Genet. 139 (2020) 291–308.
[59] C. Ji, X. Guo, Nat. Rev. Endocrinol. 15 (2019) 731–743.
[60] J.A. Bernstein, A.B. Khodursky, P.H. Lin, S. Lin-Chao, S.N. Cohen, Proc. Natl. Acad. Sci. USA 99 (2002) 9697–9702.
[61] Okazaki, J. Med. Genet. 43 (2006) e47.
[62] M. Grotzer, T. Shalaby, S. Baulande, M. Baumgartner, N. Gerber, J. Cancer Metastasis Treat. 1 (2015) 67–75.
[63] K.S. Amr, H.A.E. Atia, R.A.E. Elbnhawy, W.M. Ezzat, Genes & Diseases 4 (2017) 215–221.
[64] F. Balzano, M. Deiana, S. Dei Giudici, A. Oggiano, A. Baralla, S. Pasella, A. Mannu, M. Pescatori, B. Porcu, G. Fanciulli, Molecules 20 (2015) 19030–19040.
[65] U.S. Sandau, J.T. Wiedrick, T.J. McFarland, D.R. Galasko, Z. Fanning, J.F. Quinn, J.A. Saugstad, Sci. Rep. 14 (2024) 2148.
[66] M. Kolanowska, A. Kubiak, K. Jażdżewski, A. Wójcicka, MicroRNA analysis using next-generation sequencing, in: U.A.V. Ørom (Ed.), miRNA Biogenesis: Methods and Protocols, Springer, New York, New York, NY, 2018, pp. 87–101.
[67] Y. Hu, W. Lan, D. Miller, Next-generation sequencing for MicroRNA expression profile, in: J. Huang, G.M. Borchert, D. Dou, J. Huan, W. Lan, M. Tan, B. Wu (Eds.), Bioinformatics in MicroRNA Research, Springer, New York, New York, NY, 2017, pp. 169–177.
[68] C.-G. Liu, G.A. Calin, S. Volinia, C.M. Croce, Nat. Protoc. 3 (2008) 563–578.
[69] S. Reuben, S.A. Booth, BMC Biotechnol. 6 (2006) 47.
[70] L. Ding, C. Chen, X. Shan, B. Liu, D. Wang, Z. Du, G. Zhao, Q.P. Su, Y. Yang, B. Halkon, Adv. Mater. 36 (2024) 2308844.
[71] M. Zhang, N. Wang, Z. Li, TrAC Trends Anal. Chem. 151 (2022) 116602.
[72] P.C. Clark, E. Andresen, M.J. Sear, M. Favaro, L. Girardi, R. van de Krol, U. Resch-Genger, D.E. Starr, Small 18 (2022) 2107976.
[73] Y. Hu, B. Xu, W. Li, L. Liang, F. Fei, Q. Lin, J. Nanobiotechnol. 22 (2024) 332.
[74] C. Chen, L. Ding, B. Liu, Z. Du, Y. Liu, X. Di, X. Shan, C. Lin, M. Zhang, X. Xu, X. Zhong, J. Wang, L. Chang, B. Halkon, X. Chen, F. Cheng, F. Wang, Nano Lett. 22 (2022) 7136–7143.
[75] X. Zhu, J. Zhang, J. Liu, Y. Zhang, Adv. Sci. 6 (2019) 1901358.
[76] N. Yang, F. Gong, L. Cheng, Chem. Sci. 13 (2022) 1883–1898.
[77] S. Han, R. Deng, Q. Gu, L. Ni, U. Huynh, J. Zhang, Z. Yi, B. Zhao, H. Tamura, A. Pershin, H. Xu, Z. Huang, S. Ahmad, M. Abdi-Jalebi, A. Sadhanala, M.L. Tang, A. Bakulin, D. Beljonne, X. Liu, A. Rao, Nature 587 (2020) 594–599.
[78] A. Lay, C. Siefe, S. Fischer, R.D. Mehlenbacher, F. Ke, W.L. Mao, A.P. Alivisatos, M.B. Goodman, J.A. Dionne, Nano Lett. 18 (2018) 4454–4459.
[79] L. Zong, P. Xu, Y. Ding, K. Zhao, Z. Wang, X. Yan, R. Yu, J. Chen, X. Xing, Small 11 (2015) 2768–2773.
[80] Z. Chen, G. Liu, J. Sui, D. Li, Y. Song, F. Hong, X. Dong, J. Wang, W. Yu, Appl. Surf. Sci. 458 (2018) 931–939.
[81] D. Wei, H. Xia, L. Fang, L. Su, X. Chen, H. Song, Inorg. Chem. Front. 11 (2024) 8339–8349.
[82] C. Lee, E.Z. Xu, K.W.C. Kwock, A. Teitelboim, Y. Liu, H.S. Park, B. Ursprung, M. E. Ziffer, Y. Karube, N. Fardian-Melamed, C.C.S. Pedroso, J. Kim, S.D. Pritzl, S. H. Nam, T. Lohmueller, J.S. Owen, P. Ercius, Y.D. Suh, B.E. Cohen, E.M. Chan, P. J. Schuck, Nature 618 (2023) 951–958.
[83] Z. Jiang, L. He, Z. Yang, H. Qiu, X. Chen, X. Yu, W. Li, Nat. Commun. 14 (2023) 827.
[84] H. Zhang, Z.-H. Chen, X. Liu, F. Zhang, Nano Res. 13 (2020) 1795–1809.
[85] Z. Zhang, N. Ma, X. Kang, X. Li, S. Yao, W. Han, H. Chang, Carbohydr. Polym. 252 (2021).
[86] X. Zhao, Q. Liu, X. Li, H. Li, Z. Shen, H. Ji, T. Ma, Angew. Chem. 135 (2023) e202219214.
[87] M. Zhang, P. Huang, W. Zheng, X. Song, X. Shang, W. Zhang, D. Yang, X. Yi, X. Chen, Nano Lett. 23 (2023) 8576–8584.
[88] G. Chen, H. Qiu, P.N. Prasad, X. Chen, Chem. Rev. 114 (2014) 5161–5214.
[89] S. Fischer, N.D. Bronstein, J.K. Swabeck, E.M. Chan, A.P. Alivisatos, Nano Lett. 16 (2016) 7241–7247.
[90] J. Zhao, D. Jin, E.P. Schartner, Y. Lu, Y. Liu, A.V. Zvyagin, L. Zhang, J.M. Dawes, P. Xi, J.A. Piper, E.M. Goldys, T.M. Monro, Nat. Nanotechnol. 8 (2013) 729–734.
[91] L. Liang, D.B.L. Teh, N.-D. Dinh, W. Chen, Q. Chen, Y. Wu, S. Chowdhury, A. Yamanaka, T.C. Sum, C.-H. Chen, N.V. Thakor, A.H. All, X. Liu, Nat. Commun. 10 (2019) 1391.
[92] Y. Li, Y. Zhou, X. Yue, Z. Dai, Adv. Healthc. Mater. 9 (2020) 2001327.
[93] Z. Dang, X. Liu, Y. Du, Y. Wang, D. Zhou, Y. Zhang, S. Zhu, Adv. Mater. 35 (2023) 2306773.
[94] C.N. Thomas, N. Alfahad, N. Capewell, J. Cowley, E. Hickman, A. Fernandez, N. Harrison, O.S. Qureshi, N. Bennett, N.M. Barnes, A.D. Dick, C.J. Chu, X. Liu, A. K. Denniston, M. Vendrell, L.J. Hill, Biosens. Bioelectron. 216 (2022) 114623.
[95] J. Wu, S. Zaccara, D. Khuperkar, H. Kim, M.E. Tanenbaum, S.R. Jaffrey, Nat. Methods 16 (2019) 862–865.
[96] M. Chen, Z. Feng, X. Fan, J. Sun, W. Geng, T. Wu, J. Sheng, J. Qian, Z. Xu, Nat. Commun. 13 (2022) 6643.
[97] D. Yang, Z. Cui, Z. Wen, Z. Piao, H. He, X. Wei, L. Wang, S. Mei, W. Zhang, R. Guo, ACS Macro Lett. 5 (2023) 985–1008.
[98] S. Qu, Q. Jia, Z. Li, Z. Wang, L. Shang, Sci. Bull. 67 (2022) 1274–1283.
[99] K.R. Mun, J. Kyhm, J.Y. Lee, S. Shin, Y. Zhu, G. Kang, D. Kim, R. Deng, H.S. Jang, Nano Lett. 23 (2023) 3014–3022.
[100] Y. Kuang, T. Li, T. Jia, A. Gulzar, C. Zhong, S. Gai, F. He, P. Yang, J. Lin, Small 16 (2020) 2003799.
[101] C. Chen, F. Wang, S. Wen, Q.P. Su, M.C.L. Wu, Y. Liu, B. Wang, D. Li, X. Shan, M. Kianinia, I. Aharonovich, M. Toth, S.P. Jackson, P. Xi, D. Jin, Nat. Commun. 9 (2018) 3290.
[102] B. Amouroux, A. Eftekhari, C. Roux, J.-C. Micheau, P. Roblin, M. Pasturel, F. Gauffre, C. Würth, U. Resch-Genger, M. Sliwa, A. Bouchet, C. Coudret, Adv. Opt. Mater. 12 (2024) 2303283.
[103] Z. Pan, Y. Wen, T. Wang, K. Wang, Y. Teng, K. Shao, J. Rare Earths 38 (2020) 362–368.
[104] J.F.-C. Loo, Y.-H. Chien, F. Yin, S.-K. Kong, H.-P. Ho, K.-T. Yong, Coord. Chem. Rev. 400 (2019) 213042.
[105] X. Liang, X. Wang, J. Zhuang, Q. Peng, Y. Li, Inorg. Chem. 46 (2007) 6050–6055.
[106] M. Zhang, H. Fan, B. Xi, X. Wang, C. Dong, Y. Qian, J. Phys. Chem. C 111 (2007) 6652–6657.
[107] G. Ji, Y. Wang, Y. Qin, Y. Peng, S. Li, D. Han, S. Ren, K. Qin, S. Li, Z. Gao, T. Han, Nanotechnol. Rev. 11 (2022) 2101–2122.
[108] J. Wu, S. Du, Y. Wang, J. Mater. Chem. B 7 (2019) 7306–7313.
[109] H. Chang, J. Xie, B. Zhao, B. Liu, S. Xu, N. Ren, X. Xie, L. Huang, W. Huang, Nanomaterials 5 (2014) 1–25.
[110] Y. Ma, M. Song, L. Li, X. Lao, Y. Liu, M.-C. Wong, M. Yang, H. Chen, J. Hao, Biosens. Bioelectron. 243 (2024) 115778.
[111] Z. Li, Y. Li, Y. Wang, H. Miao, Y. Du, H. Liu, J. Alloys Compd. 613 (2014) 18–24.
[112] D. Mendez-Gonzalez, P.P. Silva-Ibáñez, F. Valiente-Dies, O.G. Calderón, J. L. Mendez-Gonzalez, M. Laurenti, A. Egatz-Gómez, E. Díaz, J. Rubio-Retama, S. Melle, J. Colloid Interface Sci. 596 (2021) 64–74.
[113] H. Li, X. Liu, X. Li, RSC Adv. 9 (2019) 42163–42171.
[114] H.P. Zhou, C.H. Xu, W. Sun, C.H. Yan, Adv. Funct. Mater. 19 (2009) 3892–3900.
[115] C. Zhang, L. Sun, Y. Zhang, C. Yan, J. Rare Earths 28 (2010) 807–819.
[116] L. Wang, C. Gao, K. Liu, Y. Liu, L. Ma, L. Liu, X. Du, J. Zhou, Adv. Funct. Mater. 26 (2016) 3480–3489.
[117] C. Wang, L. Cheng, Y. Liu, X. Wang, X. Ma, Z. Deng, Y. Li, Z. Liu, Adv. Funct. Mater. 23 (2013) 3077–3086.
[118] Y. Wang, J. Wu, M. Chen, J. Zhang, X. Sun, H. Zhou, Z. Gao, Biosens. Bioelectron. 250 (2024) 116094.
[119] G. Jin, R. He, Q. Liu, M. Lin, Y. Dong, K. Li, B.Z. Tang, B. Liu, F. Xu, Theranostics 9 (2019) 246–264.
[120] Y. He, S. Guo, Y. Zhang, Y. Liu, H. Ju, ACS Appl. Mater. Interfaces 13 (2021) 14951–14963.
[121] M. Wang, Y. Han, X. Yu, L. Liang, H. Chang, D.C. Yeo, C. Wiraja, M.L. Wee, L. Liu, X. Liu, C. Xu, Adv. Healthc. Mater. 9 (2020) 1900635.
[122] E.R. Westra, D.C. Swarts, R.H.J. Staals, M.M. Jore, S.J.J. Brouns, J. van der Oost, Annu. Rev. Genet. 46 (2012) 311–339.
[123] Y. Ishino, H. Shinagawa, K. Makino, M. Amemura, A. Nakata, J. Bacteriol. 169 (1987) 5429–5433.
[124] F. Ran, P.D. Hsu, J. Wright, V. Agarwala, D.A. Scott, F. Zhang, Nat. Protoc. 8 (2013) 2281–2308.
[125] P. Mali, L. Yang, K.M. Esvelt, J. Aach, M. Guell, J.E. DiCarlo, J.E. Norville, G. M. Church, Science 339 (2013) 823–826.
[126] K. Pardee, A.A. Green, M.K. Takahashi, D. Braff, G. Lambert, J.W. Lee, T. Ferrante, D. Ma, N. Donghia, M. Fan, Cell 165 (2016) 1255–1266.
[127] S.-Y. Li, Q.-X. Cheng, J.-M. Wang, X.-Y. Li, Z.-L. Zhang, S. Gao, R.-B. Cao, G.-P. Zhao, J. Wang, Cell Discov. 4 (2018) 20.
[128] J.S. Chen, E. Ma, L.B. Harrington, M. Da Costa, X. Tian, J.M. Palefsky, J. A. Doudna, Science 360 (2018) 436–439.
[129] J.S. Gootenberg, O.O. Abudayyeh, J.W. Lee, P. Essletzbichler, A.J. Dy, J. Joung, V. Verdine, N. Donghia, N.M. Daringer, C.A. Freije, Science 356 (2017) 438–442.
[130] C. Myhrvold, C.A. Freije, J.S. Gootenberg, O.O. Abudayyeh, H.C. Metsky, A. F. Durbin, M.J. Kellner, A.L. Tan, L.M. Paul, L.A. Parham, Science 360 (2018) 444–448.
[131] O.O. Abudayyeh, J.S. Gootenberg, S. Konermann, J. Joung, I.M. Slaymaker, D. B. Cox, S. Shmakov, K.S. Makarova, E. Semenova, L. Minakhin, Science 353 (2016) aaf5573.
[132] L. Guan, J. Peng, T. Liu, S. Huang, Y. Yang, X. Wang, X. Hao, Anal. Chem. 95 (2023) 17708–17715.
[133] J. Huang, K. Cui, L. Li, X. Li, F. Wang, Y. Wang, Y. Zhang, S. Ge, J. Yu, Langmuir 39 (2023) 16048–16059.
[134] D.C. Swarts, M. Jinek, Mol. Cell 73 (2019) 589–600, e584.
[135] W. Zhao, X. Zhang, R. Tian, H. Li, S. Zhong, R. Yu, Sensors Actuators B Chem. 393 (2023) 134238.
[136] P. Miao, Y. Sun, G. Zheng, B. Wang, W. Wang, J. Zhang, M. Yan, Y. Lv, J. Colloid Interface Sci. 667 (2024) 82–90.

[137] T. Gu, Z. Ren, X. Li, J. Huang, G. Han, Chem. Commun. 55 (2019) 9104–9107.
[138] C. Chen, S. Hu, L. Tian, M. Qi, Z. Chang, L. Li, L. Wang, B. Dong, Biosens. Bioelectron. 252 (2024) 116135.
[139] L. Mao, Z. Lu, N. He, L. Zhang, Y. Deng, D. Duan, Sci. China Chem. 60 (2017) 157–162.
[140] S. Kuusinen, S. Lahtinen, T. Soukka, Analysis & Sensing 4 (2024) e202400005.
[141] V. Muhr, C. Würth, M. Kraft, M. Buchner, A.J. Baeumner, U. Resch-Genger, T. Hirsch, Anal. Chem. 89 (2017) 4868–4874.
[142] M.C. Dos Santos, W.R. Algar, I.L. Medintz, N. Hildebrandt, TrAC Trends Anal. Chem. 125 (2020) 115819.
[143] G. Ramírez-García, M.Á. Honorato-Colin, E. De la Rosa, T. López-Luke, S. S. Panikar, J. de Jesús Ibarra-Sánchez, V. Piazza, J. Photochem. Photobiol. A Chem. 384 (2019) 112053.
[144] B. Guven, F.C. Dudak, I.H. Boyaci, U. Tamer, M. Ozsoz, Analyst 139 (2014) 1141–1147.
[145] C.-C. Lin, C.-W. Chang, Biosens. Bioelectron. 51 (2014) 297–303.
[146] M. Zacharias, J. Phys. Chem. B 124 (2020) 10345–10352.
[147] P. Yakovchuk, E. Protozanova, M.D. Frank-Kamenetskii, Nucleic Acids Res. 34 (2006) 564–574.
[148] X.-X. Peng, T. Guo, H. Lu, L. Yue, Y. Li, D. Jin, G.-J. Zhang, F. Yang, ACS sens 5 (2020) 2514–2522.
[149] S. Wu, H. Chen, Z. Zuo, M. Wang, R. Luo, H. Xu, Int. J. Electrochem. Sci. 10 (2015) 3848–3858.
[150] B. Liu, S. Salgado, V. Maheshwari, J. Liu, Curr. Opin. Colloid Interface Sci. 26 (2016) 41–49.
[151] L. Gao, C. Lian, Y. Zhou, L. Yan, Q. Li, C. Zhang, L. Chen, K. Chen, Biosens. Bioelectron. 60 (2014) 22–29.
[152] A.M. Kotulska, A. Pilch-Wróbel, S. Lahtinen, T. Soukka, A. Bednarkiewicz, Light Sci. Appl. 11 (2022) 256.
[153] J. Hu, F. Zhao, H. Ling, Y. Zhang, Q. Liu, Nanoscale Adv. 6 (2024) 2945–2953.
[154] G. Yang, Y. Liu, J. Teng, C.-X. Zhao, Biosensors 11 (2021) 505.
[155] Y. Wang, M. Lv, Z. Chen, Z. Deng, N. Liu, J. Fan, W. Zhang, Front. Chem. 8 (2020) 238.
[156] Y. Rong, H. Li, Q. Ouyang, S. Ali, Q. Chen, Spectrochim. Acta, Part A 239 (2020) 118500.
[157] W. Gang, F. Yike, R. Zhaohui, H. Jie, B. Serena, L. Xiang, H. Gaorong, Chem. Commun. 54 (2018) 6324–6327.
[158] M. Sonia, C.O. Gómez, L. Marco, M.G. Diego, E.G. Ana, L.C. Enrique, C. G. Eduardo, D. Elena, R.R. Jorge, J. Phys. Chem. C 122 (2018) 18751–18758.
[159] J.A. Broussard, B. Rappaz, D.J. Webb, C.M. Brown, Nat. Protoc. 8 (2013) 265–281.
[160] S. Chen, Y.L. Yu, Fluorescence resonance energy transfer (FRET) spectroscopy, in: P. Worsfold, C. Poole, A. Townshend, M. Miró (Eds.), Encyclopedia of Analytical Science (Third Edition), Academic PressAcademic Press, Oxford, 2019, pp. 341–348.
[161] W.C. Yang, S.Y. Li, S. Ni, G. Liu, Aggregate 5 (2024) e460.
[162] M. Lunz, A.L. Bradley, V.A. Gerard, S.J. Byrne, Y.K. Gun'Ko, V. Lesnyak, N. Gaponik, Phys. Rev. B 83 (2011) 52–57.
[163] A.K. Verma, A. Noumani, A.K. Yadav, P. Solanki, Diagnostics 13 (2023) 1375.
[164] S.A.E. Marras, K.F. Russell, T. Sanjay, Nucleic Acids Res. 30 (2002) e122.
[165] M.K. Johansson, M.K. Cook, Chem. Eur. J. 9 (2003) 3466–3471.
[166] Y. He, H. Rao, J. Wang, Y. Wu, C. Han, C. Yan, H. Temple, L. Zhang, W. Chen, Y. Liu, Cancer Nanotechnol. 14 (2023) 52.
[167] K. Zhang, N. Zhang, Y. Wu, W. Zhang, F. Li, Y. Shen, Sensors Actuators B Chem. 342 (2021) 130062.
[168] L. Frances-Soriano, N. Estebanez, J. Perez-Prieto, N. Hildebrandt, Adv. Funct. Mater. 32 (2022) 2201541.
[169] M. Laurenti, M. Paez-Perez, M. Algarra, P. Alonso-Cristobal, E. Lopez-Cabarcos, D. Mendez-Gonzalez, J. Rubio-Retama, ACS Appl. Mater. Interfaces 8 (2016) 12644–12651.
[170] S. Li, L. Xu, W. Ma, X. Wu, M. Sun, H. Kuang, L. Wang, N.A. Kotov, C. Xu, J. Am. Chem. Soc. 138 (2016) 306–312.
[171] T.C. De Bang, P. Shah, S.K. Cho, S.W. Yang, S. Husted, Anal. Chem. 86 (2014) 6823–6826.
[172] S. Zhang, R. Liu, Z. Xing, S. Zhang, X. Zhang, Chem. Commun. 52 (2016) 14310–14313.
[173] Q. Kang, M. He, B. Chen, G. Xiao, B. Hu, Anal. Chem. 93 (2020).
[174] S.R. David, M.B. Inmaculada, G. Ana, C. Pablo, F. Marta, K. Abdelnaby, J. M. Marin, Sci. Rep. 8 (2018) 10306.
[175] D. Poel, T.E. Buffart, J. Oosterling-Jansen, H.M. Verheul, J. Voortman, Exp. Mol. Med. 50 (2018) e454.
[176] G. Charlotte, C. Sebastian, B. Kim, J. Reza, J. Javad, R. Bjarke, T. Philipp, H. Bianca, K.B. Stefan, W. Reza, PLoS One 12 (2017) e0167969.
[177] A. Maiese, A. Scatena, A. Costantino, M. Di Paolo, R. La Russa, E. Turillazzi, P. Frati, V. Fineschi, Diagnostics 11 (2021) 64.
[178] E. Boštjančič, N. Zidar, D. Štajer, D. Glavač, Cardiology 115 (2010) 163–169.